Thrust Removal Methodology for the FAST-MAC Circulation Control Model Tested in the National Transonic Facility

David T. Chan[∗], William E. Milholen, II[†], Gregory S. Jones[‡], and Scott L. Goodliff[§]

NASA Langley Research Center, Hampton, VA, 23681

A second wind tunnel test of the FAST-MAC circulation control semi-span model was recently completed in the National Transonic Facility at the NASA Langley Research Center. The model allowed independent control of four circulation control plenums producing a high momentum jet from a blowing slot near the wing trailing edge that was directed over a 15% chord simple-hinged flap. The model was configured for transonic testing of the cruise configuration with 0° flap deflection to determine the potential for drag reduction with the circulation control blowing. Encouraging results from analysis of wing surface pressures suggested that the circulation control blowing was effective in reducing the transonic drag on the configuration, however this could not be quantified until the thrust generated by the blowing slot was correctly removed from the force and moment balance data. This paper will present the thrust removal methodology used for the FAST-MAC circulation control model and describe the experimental measurements and techniques used to develop the methodology. A discussion on the impact to the force and moment data as a result of removing the thrust from the blowing slot will also be presented for the cruise configuration, where at some Mach and Reynolds number conditions, the thrust-removed corrected data showed that a drag reduction was realized as a consequence of the blowing.

Nomenclature

Symbols

A_{exit}	Slot exit area, in^2	C_μ	Momentum thrust coefficient
AF	Axial Force, lbf	C_{dis}	Nozzle discharge coefficient
$A\!R$	Aspect ratio	$C_{F_{mom}}$	Non-dimensional momentum thrust
b	Wing span, in	$C_{F_{pres}}$	Non-dimensional pressure thrust
c	Local wing chord, in	$C_{F_{total}}$	Non-dimensional total thrust
$\overline{c}$	Mean aerodynamic chord, in	F_{mom}	Momentum thrust, lbf
C_A	Axial force coefficient	F_{pres}	Pressure thrust, lbf
C_D	Drag coefficient	F_R	Resultant thrust, lbf
C_L	Lift coefficient	F_{total}	Total thrust, lbf
C_l	Rolling moment coefficient	g	Standard gravitational acceleration
C_m	Pitching moment coefficient		($=32.174$ ft/sec^2)
C_N	Normal force coefficient	h	Blowing slot height, in
C_n	Yawing moment coefficient	M	Local Mach number
C_T	Total thrust coefficient	M_∞	Freestream Mach number
C_Y	Side force coefficient	NF	Normal force, lbf
		NPR	Nozzle pressure ratio, (p_o/p_∞)
		$NPR_{critical}$	Critical nozzle pressure ratio for sonic

[∗]Research Aerospace Engineer. Configuration Aerodynamics Branch. Mail Stop 499. Member AIAA.

[†]Research Aerospace Engineer. Configuration Aerodynamics Branch. Mail Stop 499. Senior Member AIAA.

[‡]Research Aerospace Engineer. Configuration Aerodynamics Branch. Mail Stop 267. Senior Member AIAA.

[§]Test Engineer. Jacobs Technology, Inc. Mail Stop 267. Member AIAA.

American Institute of Aeronautics and Astronautics

	condition (=1.893 for γ=1.4)
NPR_{exit}	Nozzle exit pressure ratio, (p_o/p_{exit})
p_∞	Freestream static pressure, psi
p_b	Ambient back pressure, psi
p_{exit}	Slot exit static pressure, psi
p_o	Stagnation pressure, psi
p_t	Tunnel stagnation pressure, psi
PM	Pitching moment, in-lbf
q_∞	Freestream dynamic pressure, psf
r_1	Flap radius 1
r_2	Flap radius 2
R_{air}	Specific gas constant for dry air (=53.3533 ft-lbf/lbm-°R)
Re	Reynolds number based on mean aerodynamic chord
RM	Rolling Moment, in-lbf
S_{ref}	Wing reference area, ft^2
SF	Side Force, lbf
T_o	Stagnation temperature, °R
T_s	Static temperature, °R
T_t	Tunnel stagnation temperature, °F
U	Local velocity, ft/sec
$\dot{w}$	Weight flow rate, lbm/sec
$\overline{x}$	X moment transfer distance, in
$\overline{y}$	Y moment transfer distance, in
YM	Yawing Moment, in-lbf
$\overline{z}$	Z moment transfer distance, in
α	Angle of attack, deg
Δ	denotes increment or difference
γ	Ratio of specific heats (=1.4 for dry air)
ψ	Yaw angle, deg
ρ	Density, lbm/ft^3
θ	Pitch angle, deg

Subscripts

o	Stagnation quantity
∞	Freestream quantity
bal	Balance measurement
$exit$	Slot exit location
$ideal$	Ideal calculation based on one-dimensional isentropic equations
jet	Jet quantity
MCV	MCV measurement
$meas$	Measured quantity
$thrust$	Thrust quantity

$total$	Total quantity
TR	Thrust-removed quantity
$wideal$	Calculated using ideal weight flow rate
$wmeas$	Calculated using measured weight flow rate

Units

°, deg	degrees
°F	degrees Fahrenheit
°R	degrees Rankine
atm	atmospheres
cts	counts (0.0001)
ft	feet
in	inches
lbf	pounds force
lbm	pounds mass
M	million, 1x10^6
psf	pounds per square foot
psi	pounds per square inch
sec	seconds

Acronyms

AIAA	American Institute of Aeronautics and Astronautics
BCRS	Balance Cavity Recirculation System
BMC	Balance Moment Center
CFD	Computational Fluid Dynamics
EU	Engineering Units
FAST-MAC	Fundamental Aerodynamics Subsonic/Transonic-Modular Active Control
FS	Full-Scale
HPA	High Pressure Air
LaRC	Langley Research Center
MCV	Multiple Critical Venturi
MRC	Moment Reference Center
NASA	National Aeronautics and Space Administration
NTF	National Transonic Facility
OML	Outer Mold Line
OTW	Over the Wing
PCV	Pressure Control Valve
PIP	Pressure Interface Piece
SMSS	Sidewall Model Support System
STOL	Short Take-Off and Landing
WT	Wind Tunnel

American Institute of Aeronautics and Astronautics

I.   Introduction

MANY of the advanced future aircraft being designed today utilize advanced propulsion and active flow control systems that closely integrate the engine and airframe.[1–6] Cruise efficiency, community noise, and runway independence can no longer be optimized independently because of the close coupling of the engine, airframe, and wing. Circulation control techniques have experienced a resurgence recently, with many research efforts focusing on developing databases for CFD validation,[7–13] as unreliable predictions have been a barrier to applying the techniques to aircraft. The lack of Reynolds number scaling data is also a shortfall of many active flow control datasets.

Evaluating the benefits of active flow control systems on scaled wind tunnel models requires added attention to detail. Not only does the outer mold line of the model need to accurately represent the proposed flight vehicle, but also the intricate details of the flow control system. Additionally, if the flow control system adds a net thrust to the flow field, it is necessary to accurately characterize the static thrust produced in order to remove its effect and isolate the induced aerodynamic effects of the flow control system. It is also desirable that the wind tunnel testing be conducted at Reynolds numbers that are representative of flight conditions, to document the appropriate scaling parameters, and ensure the active flow control technique is properly scaled to the flight vehicle.

The circulation control method that is discussed throughout the paper is one where a high momentum jet from a blowing slot near the wing trailing edge is tangentially ejected over the curved surface of a simple short-chord hinged flap (Figure 1). The Coandă effect causes the jet to remain attached to the curved surface because of a balance between the low static pressures in the jet sheet and the centrifugal force around the curvature of the surface.[14, 15] For circulation control applications, the jet flow is typically characterized at the exit of the blowing slot by the non-dimensional jet momentum coefficient C_μ. The non-dimensional slot height (h/c), the plenum stagnation conditions $\left((p_o)_{jet}, (T_o)_{jet} \right)$, and the weight flow rate $(\dot{w}_{jet})$ are the key measurements to be made to quantify C_μ. In addition, the slot exit static pressure (p_{exit}) is needed to complete the calculation of the total thrust produced at the slot exit.
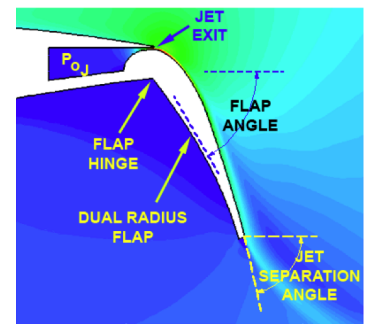

Figure 1.   Circulation control blowing example.

A second active flow control experiment (Test 213) was recently conducted in the National Transonic Facility (NTF), shown in Figure 2(a), at the NASA Langley Research Center (LaRC). The Fundamental Aerodynamics Subsonic/Transonic-Modular Active Control (FAST-MAC) model was again used to test circulation control concepts at realistic flight Reynolds numbers at both low-speed and transonic cruise conditions, building upon the successes of the first test entry (NTF Test 195).[16] The FAST-MAC model has a super-critical wing and represents an advanced configuration that is characteristic of modern aircraft. The geometry and results of the high Reynolds number tests in the NTF can be openly distributed to the research community to aid in CFD validation. The model is also unique in that it integrates circulation control strategies to be evaluated at transonic Mach numbers, where little research has been published except on two-dimensional airfoils.[15, 17, 18] Figure 2(b) shows a photograph of the FAST-MAC model installed in the NTF test section.

(a) Aerial view of the NTF.
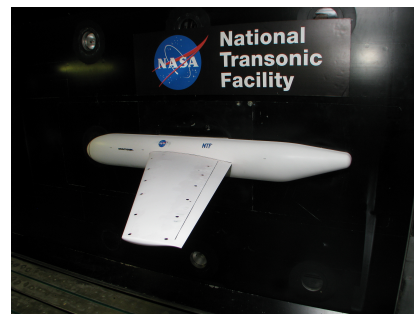
(b) FAST-MAC model in cruise configuration in the NTF.

Figure 2.   National Transonic Facility and FAST-MAC model.

The model was tested over a wide range of Mach and Reynolds numbers to investigate the effect of various circulation control techniques. This second test entry of the FAST-MAC model resulted in significant improvements in data quality, particularly in the transonic speed range. These results were documented in recent AIAA papers.[19,20] An analysis of the wing surface pressures revealed that for attached flow conditions at M_∞=0.85, the circulation control blowing increased the lift and moved the shockwave aft on the wing, without changing the strength of the shockwave. At the off-design conditions at M_∞=0.88, the blowing was effective in re-attaching the shock-induced flow separation, moving the shockwave aft approximately 5% chord with no increase in shockwave strength. These encouraging results suggest that the circulation control blowing was effective in reducing the transonic drag on the configuration, however this cannot be quantified until the thrust generated by the blowing slot is correctly removed from the force and moment balance data.

The intent of this paper is to present the thrust removal methodology used for the FAST-MAC circulation control model. Section II describes the experimental setup for the FAST-MAC tests in the NTF, which includes descriptions of the various measurements needed for thrust removal. Section III provides details on the development of the thrust removal methodology for the FAST-MAC model, and also includes a summary of thrust removal methods used in historical propulsion and flow control simulation experiments. Finally, in Section IV, a discussion on the impact to the wind-on force and moment data due to the removal of static thrust, is presented. The lift and drag increments due to the induced effects of the blowing slot are quantified for the cruise configuration.

II.   Experimental Setup

A.   Wind Tunnel Description

The NTF is one of a limited number of wind tunnel facilities that can achieve flight Reynolds numbers and Mach numbers for transport type aircraft for both cruise and high lift operations.[21] The tunnel is a fan-driven, closed-circuit, continuous-flow, pressurized wind tunnel capable of operating either in dry air at warm temperatures up to 120°F or in nitrogen gas from warm to cryogenic temperatures down to -270°F. Figure 3 shows the major components of the NTF tunnel circuit, including the location of the sidewall model support system (SMSS) used for semi-span model testing and the location of the high pressure air (HPA) de-

Figure 3. Major components of the NTF tunnel circuit including the SMSS and Air Station (linear dimensions in feet).

livery station needed for propulsion simulation and flow control experiments. The HPA station has two multiple critical venturi (MCV) systems to measure the total weight flow rate through the system. The SMSS houses the large external force and moment balance and also houses the Pressure Interface Piece (PIP), which transfers the incoming HPA across the non-metric / metric boundary of the balance. More information about the HPA station and SMSS are found in Appendices A and B, respectively. The NTF test section is 8.2 ft by 8.2 ft in cross section and 25 ft in length. The test section floor and ceiling are slotted (6 percent open), and the sidewalls are solid. The wind tunnel is capable of an absolute pressure range from 1 atm to 9 atm, a stagnation temperature range from -270°F to 120°F, a Mach number range from 0.1 to 1.2, and a maximum Reynolds number of 146x10^6 per foot at Mach 1. For the circulation control experiment described in this paper, the temperature envelope was limited to -50°F to 120°F due to limitations in the model protection system.
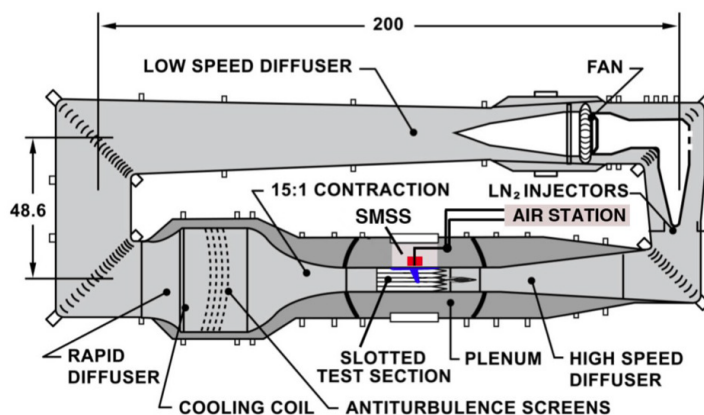
American Institute of Aeronautics and Astronautics

B.   Model Description

The FAST-MAC model shown in Figure 4 has a modern super-critical wing and was designed to become an NTF standard for evaluating performance characteristics of integrated active flow control and propulsion systems. The outer mold line (OML) of the model was designed for a cruise Mach number of 0.85 and a lift coefficient of 0.50, at a Reynolds number based on mean aerodynamic chord of 30×10^6. A tangential blowing slot is located at the 85% chord location on the upper surface, and is directed over a 15% chord simple hinged flap for both the cruise and high-lift configu-

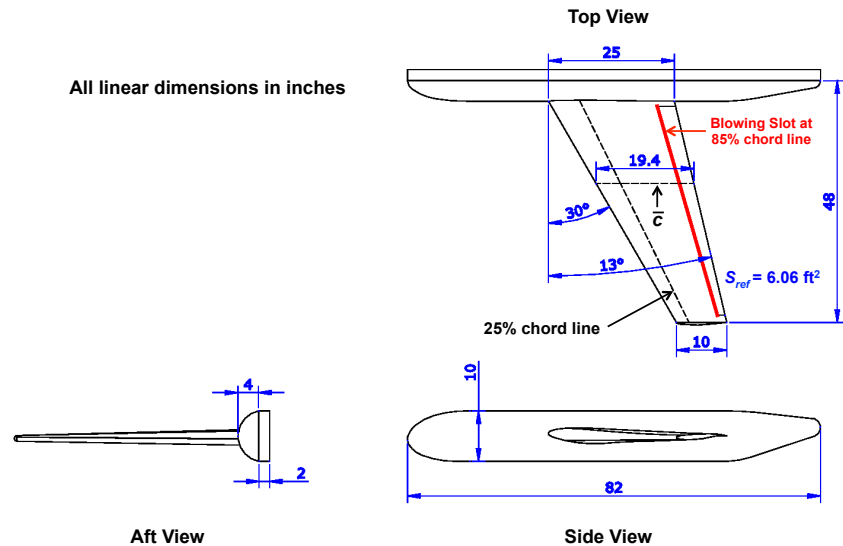**Figure 4.   3-view drawing with pertinent dimensions of the FAST-MAC semi-span model in cruise configuration.**

rations. The wing is mounted in the mid-fuselage position and has an aspect ratio of 5.28, a leading edge sweep of 30°, a half-span of 48.0 inches, a mean aerodynamic chord of 19.4 inches, and a reference area of 6.06 ft². Even though the wing has a moderate aspect ratio, it represents the state-of-the-art in transonic super-critical wing design.[22, 23] The model is offset from the tunnel sidewall using a 2.0-inch non-metric standoff,[24] which has a profile shape identical to that of the fuselage centerline. Additional details related to the FAST-MAC model design is found in Appendix C.
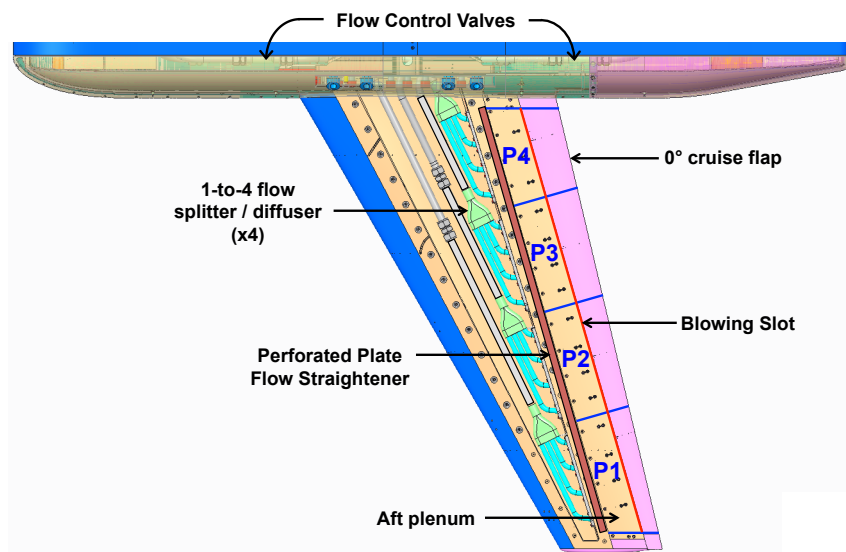
**Figure 5.   Four independent flow paths in the FAST-MAC model.**

The FAST-MAC model utilized four independent flow paths to achieve lift and thrust performance along the span of the circulation control flap as shown in Figure 5. Each plenum section had its own flow control valve located in the fuselage that fed a rapid diffuser located in the wing box. The diffuser is used to subdivide the incoming flow to the plenum, allowing it to be supplied at four evenly spaced span wise locations. Each plenum had four perforated plates (17% open area) designed to maintain flow uniformity into the aft plenum settling chamber.[20] The flow then enters the aft plenum region of the model,

where the upper plenum cover is supported by streamlined standoffs, which are used to set the blowing slot height. The aft section of the plenum had a 6-to-1 contraction ratio to the jet exit for the $h/c = 0.0032$ configuration and a contraction ratio of 12-to-1 for the $h/c = 0.0021$ configuration. For each configuration, care was given to accurately set and measure the slot exit areas for each plenum, as this plays an important role in computing the added thrust.

American Institute of Aeronautics and Astronautics

C. Experimental Measurements

The total instrumentation package for the FAST-MAC model will not be discussed here, however the measurements that are needed for the thrust removal methodology and the instrumentation to acquire these measurements are described in the following sections.

1. Internal Flow Path Measurements

The weight flow rate and thrust from the blowing slot are calculated assuming a one-dimensional isentropic expansion from measured stagnation conditions. In each plenum, there are two pitot probes to measure the stagnation pressure and two thermocouples on the probes to measure the stagnation temperature. The two measurements are averaged to produce the stagnation quantities to be used in the isentropic equations. Additionally, one surface pressure tap on the flap for each plenum is used to measure the slot exit static pressure. These are used to check the behavior of the slot exit and are used to calculate the pressure thrust component of the total thrust from the slot exit.
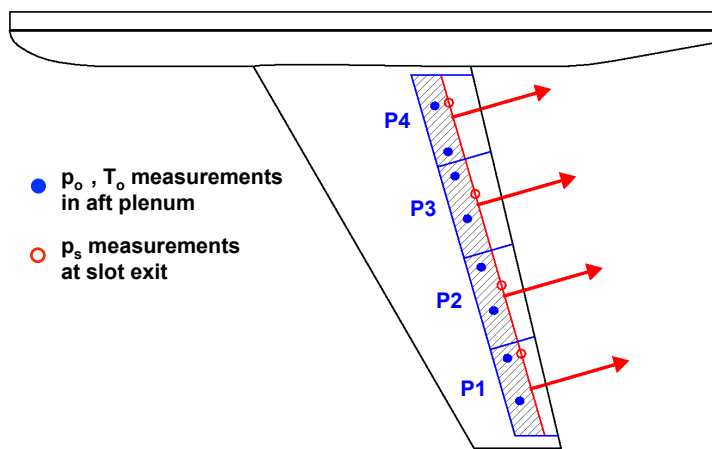
Figure 6. Locations of measured stagnation quantities and static exit pressure for each plenum.

Figure 6 shows a planform view of the FAST-MAC model and the locations of the stagnation pressure and temperature measurements in each plenum and the static pressure measurements on the flap at the slot exit. Figure 7 shows section cuts normal to the slot at the flap pressure row for plenum #4 as an example. The design intent was to locate one of the static pressure taps from each row to be at the apex of the first flap radius that corresponds to the jet exit plane. However, due to space limitations and machining uncertainty, some of the taps are not lined up with the slot exit, especially for the 30° and 60° flap configurations. This introduces uncertainty in these measurements and the effect will be shown in a later section.

| (a) Section cut location | (b) 0° flap, Plenum 4 | (c) 30° flap, Plenum 4 | (d) 60° flap, Plenum 4 |
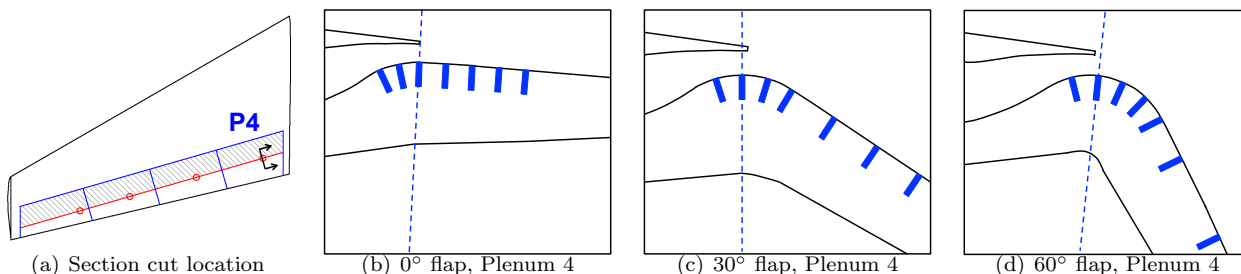
Figure 7. Section cuts normal to the slot of the aft plenum and flap detailing the locations of the static pressure taps. Plenum #4 of the $h/c = 0.0021$ configuration shown as an example.

2. Slot Height Measurements

The slot area is an important parameter in the calculation of jet weight flow rate and momentum thrust. It is very important to measure the slot height to verify the desired h/c and to obtain a good calculation of the total slot area. The uncertainty in these measurements contributes to the uncertainty of the calculated weight flow rate and momentum thrust. To calculate the slot areas for each plenum, the slot height was measured at each standoff location along the span of the slot using precision pin gauges. The slot areas for all flap configurations are listed in Table 1. Additional details are found in Appendix D. Furthermore, during

American Institute of Aeronautics and Astronautics

the first test entry of the FAST-MAC model, an electronic slot height gauge capable of providing real-time measurements was used to show that the slot height did not vary when the plenums were pressurized.

Table 1. Measured plenum slot areas for each flap and h/c configuration for the FAST-MAC model.

Flap Angle, deg	Slot Design Constant	Plenum A_{exit} , in^2				
		1	2	3	4	Total
0	$h/c = 0.0021$	0.3600	0.3973	0.4923	0.6256	1.8752
30	$h/c = 0.0021$	0.3532	0.3963	0.4918	0.5734	1.8147
30	$h = 0.041$ in	0.4403	0.4479	0.4465	0.4692	1.8039
60	$h/c = 0.0021$	0.3341	0.4024	0.4789	0.5705	1.7859
60	$h/c = 0.0032$	0.5059	0.5915	0.7334	0.8000	2.6308

3. Total Weight Flow Rate Measurement

The NTF Air Station (Figure 26) has two multiple critical venturi (MCV) systems[25] to capture the total weight flow rate from each flow path leg. The high flow leg was the only leg utilized for the FAST-MAC series of tests. The combined uncertainty of the MCV system is reported to be less than 0.35 percent of reading.[26] Additional details about the MCV systems are found in Appendix D.

4. Force and Moment Measurements

The NTF-117S[27] balance is a large 5-component (no side force measurement capability) strain gauge balance that is mounted inside the SMSS and is the primary force measurement system for semi-span models in the NTF. The Pressure Interface Piece (PIP) allows the high-pressure supply air needed for propulsion and flow control simulation testing to "bridge" the balance by crossing from the non-metric end to the metric end. Consequently, the balance and PIP must be considered together as a system and calibrated accordingly.[28] Table 2 shows the results of this system calibration.[29] The calibration accuracies are presented both as a percentage of full-scale load and in engineering units of lbf or in-lbf. The right side of the table converts the numbers to aerodynamic coefficient accuracies at conditions for the FAST-MAC model. Additional details about the NTF-117S balance and the PIP are found in Appendix D.

Table 2. NTF-117S force measurement system calibration results (includes effect of PIP pressure and temperature).[29]

Balance Component	Calibration Load Range	Calibration Accuracy		Coefficient Accuracy for FAST-MAC Model			
		%-FS	EU	M_∞=0.85 Re=10M	M_∞=0.85 Re=30M	M_∞=0.88 Re=15M	M_∞=0.88 Re=30M
AF	1,800 lbf	0.432	7.78 lbf	0.0012	0.0006	0.0008	0.0006
NF	12,000 lbf	0.136	16.32 lbf	0.0025	0.0013	0.0017	0.0013
PM	90,000 in-lbf	0.072	64.80 in-lbf	0.0005	0.0003	0.0003	0.0003
RM	670,000 in-lbf	0.063	422.10 in-lbf	0.0014	0.0007	0.0009	0.0007
YM	110,000 in-lbf	0.182	200.20 in-lbf	0.0006	0.0003	0.0004	0.0003

III. Thrust Removal Methodology

A. Background and History

This section provides background information into the thrust removal methodology used in many historical propulsion simulation experiments. The goal is to determine whether the same methodology can be used for the FAST-MAC circulation control model and if not, develop a methodology that attempts to capture the same intent.

1. Typical Thrust Removal Techniques

In propulsion simulation wind tunnel tests, the force and moment data acquired from a strain gauge balance frequently include the effects of the static thrust from the propulsion simulator. In these cases where the thrust is metric (i.e. sensed and measured by the balance), the effect of the static thrust needs to be removed from the wind-on balance measurements to isolate the pure aerodynamic and jet-induced effects in the force and moment data.

Wind tunnel facilities that perform propulsion simulation experiments have well-established procedures for static thrust removal in their data reduction programs.[30] Typically, the balance measurements acquired during wind-off thrust tares are used to determine the static thrust as a function of NPR. The balance measurements are used to determine the total resultant thrust magnitude, the resultant in the aircraft pitch axis, and the resultant in the aircraft yaw axis as shown in Equations 1, 2, and 3, respectively. The balance measurements are also used to calculate the static thrust vector angles in the aircraft pitch and yaw axes as shown in Equations 4 and 5, respectively.

$$(F_R)_{bal}\big|_{total} = \sqrt{AF_{bal}^2 + NF_{bal}^2 + SF_{bal}^2} \tag{1}$$

$$(F_R)_{bal}\big|_{pitch} = \sqrt{AF_{bal}^2 + NF_{bal}^2} \tag{2}$$

$$(F_R)_{bal}\big|_{yaw} = \sqrt{AF_{bal}^2 + SF_{bal}^2} \tag{3}$$

$$\theta_{thrust} = \tan^{-1}\left(\frac{-NF_{bal}}{AF_{bal}}\right) \tag{4}$$

$$\psi_{thrust} = \tan^{-1}\left(\frac{-SF_{bal}}{AF_{bal}}\right) \tag{5}$$

The thrust quantities also need to be non-dimensionalized since different back pressures usually exist between the wind-off conditions and the wind-on conditions. The desire is to remove the amount of static thrust that would have been present at the back pressure of the wind-on measurements. There are two methods for obtaining non-dimensional static thrust quantities.[30, 31] The "p_b method" involves dividing the static thrust by the ambient back pressure from the thrust tare and a reference area, where the reference area is defined as the nozzle throat area or nozzle exit area. This is converted back to dimensional form in the thrust removal process by multiplying by the chosen reference area and the freestream static pressure (p_∞) of the wind-on data. The other method is called the "F_{ideal} method" and involves dividing the static thrust by the ideal isentropic thrust for the nozzle. This method requires measuring stagnation quantities in the nozzle, as well as the weight flow rate through the nozzle to calculate the ideal thrust. The "p_b method" is usually used because it is simpler and produces mostly linear curves as a function of NPR. However, by design, the "F_{ideal} method" provides a measure of the nozzle efficiency and can be used to evaluate different nozzle designs.

2. Historical Experiments

Many propulsion simulation and flow control experiments on various aircraft configurations have been performed in the past couple of decades. The chosen method for thrust removal depended on the test objectives and the test setup, where the nozzle configuration is divided into two categories, free jets or wall-bounded jets. Most experiments followed the "p_b method" for free jets unless the test setup prevented them from

doing so. Some experiments did not remove the effect of static thrust from their measurements at all, and presented their data as such.

Investigations into jet-induced effects of different exhaust nozzles (standard or vectored) on the performance of fighter aircraft,[32–36] used the standard thrust removal methods outlined above since the jet exhaust did not flow over other metric parts of the model. In some flow control investigations on short-takeoff-and-landing (STOL) aircraft, such as externally blown flaps from over-the-wing (OTW) engine simulators[37, 38] or internally blown flaps using compressed air,[39] the same thrust removal methods were used, but the thrust tares were performed without the flaps installed to remove the effects of the wall-bounded jet from the balance measurements (i.e. only the static thrust was measured).

Other experiments used alternate methods to measure the static thrust. For propulsive lift concepts studied in the LaRC 16-foot Transonic Tunnel,[40–42] a two-balance system was used where one balance would measure the thrust forces and the other balance would measure the combined thrust and aerodynamic forces. The measurements from the thrust balance would be subtracted from the other balance to obtain only the aerodynamic and jet-induced forces. In other flow control investigations on STOL aircraft, real engines were used either for OTW blowing over flaps or for internally blown flaps using engine-bleed air. In these cases, the static thrust was determined pre-test on an engine test stand.[43–45]

In many of these historical experiments on aircraft propulsion concepts, the scale wind tunnel data is combined with real engine data in order to predict full-scale aircraft performance. The real engine data is always provided in terms of static uninstalled thrust at the static uninstalled vector angle, therefore the wind tunnel data must be based on removal of static thrust at the static vector angle as opposed to wind-on thrust at the wind-on vector angle.[31] This is especially important for applications such as circulation control blowing since the wind-on effective thrust vector angle is significantly different than the static vector angle.

B.   Thrust Removal for FAST-MAC

For the FAST-MAC model, in order to remove the effects of the blowing slot static thrust from the wind-on force and moment balance measurements, the static thrust at wind-off conditions must first be measured or calculated. The measured forces and moments from the balance acquired during a wind-off thrust tare can be used to determine the components of the static thrust similar to the historical method described earlier. However, to isolate the pure static thrust effects, the blowing slot would be required to exhaust straight out into the ambient back pressure (free jet) and not over a metric part of the model (wall-bounded jet). Unfortunately, since the blowing slot is directed over the flap, the balance cannot distinguish between the static thrust effect and the aerodynamic Coandă effect of the wall-bounded jet and would instead measure the combined effect. In some of the historical experiments, the flap was removed to conduct the static thrust tares, but that could not be done for the FAST-MAC model because in the current design, the flap model part is integral to setting of the blowing slot height. A redesign of the complex internal flow paths would be required to change this. Therefore, it was concluded that the balance data from the wind-off thrust tares could not be used to determine the pure static thrust effects until a thrust calibration fixture is designed and implemented.

The alternative would be to use the measured stagnation quantities in each plenum to calculate the ideal thrust from the blowing slot assuming a one-dimensional isentropic expansion. The resultant thrust can then be resolved along the x, y, and z directions if the thrust vector angles are known. However, the calculated quantities would need to be corrected for viscous effects. This would be done by cal-

Figure 8.   Measured and Calculated Internal Flow Quantities.

culating a nozzle discharge coefficient or nozzle efficiency factor that relates the measured weight flow rate

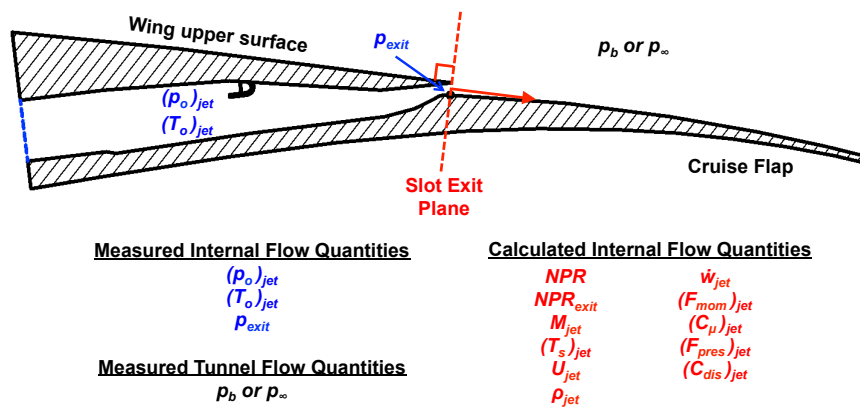from the MCV to the ideal weight flow rate calculated from the measured stagnation quantities. This would scale the calculated thrust accordingly to account for viscous effects ignored by the isentropic equations. This is the method that is used for the FAST-MAC model and the thrust is calculated at the slot exit plane as illustrated in Figure 8. Note that the slot exit plane is normal to the wing upper surface by design. Any effect that occurs after the slot exit plane is considered an aerodynamic effect and not a static thrust effect and is bookkept accordingly. Therefore, the turning of the jet onto the flap due to the Coandă effect of the wall-bounded jet is NOT included as part of the static thrust.

1. Internal Flow Equations

Using the measured stagnation pressure and temperature inside the plenum just upstream of the slot exit as shown in Figure 8, isentropic equations for an ideal gas are used to calculate the thrust out of each plenum as the jet is assumed to expand adiabatically to the free stream static pressure. The following set of equations are used for each plenum, so there are a total of four sets of calculated flow quantities such as $M_{jet}\big|_{1-4}$.

The classical definition of nozzle pressure ratio (NPR) is shown in Equation 6. The pressure ratio at the slot exit (NPR_{exit}) is shown in Equation 7 and is different than the classical definition of NPR due to influences of the wall-bounded jet. The value listed for $NPR_{critical}$ in Equation 8 represents the minimum pressure ratio for choked flow to occur.

$$NPR = \frac{(p_o)_{jet}}{p_\infty} \tag{6}$$

$$NPR_{exit} = \frac{(p_o)_{jet}}{p_{exit}} \tag{7}$$

$$NPR_{critical} = 1.893 \tag{8}$$

The jet Mach number at the slot exit is calculated using Equation 9 and it has a maximum value of 1 once the NPR reaches $NPR_{critical}$ and a choked flow condition is established at the slot exit.

$$M_{jet} = \sqrt{\left(\frac{2}{\gamma_{jet} - 1}\right)\left(NPR^{\left(\frac{\gamma_{jet} - 1}{\gamma_{jet}}\right)} - 1\right)} \qquad \text{for } NPR < NPR_{critical} \tag{9a}$$

$$M_{jet} = 1 \qquad \text{for } NPR \geq NPR_{critical} \tag{9b}$$

The jet static temperature, jet velocity, and jet density are calculated using Equations 10, 11, and 12, respectively.

$$(T_s)_{jet} = \frac{(T_o)_{jet}}{1 + \left(\frac{\gamma_{jet} - 1}{2}\right) M_{jet}^2} \tag{10}$$

$$U_{jet} = M_{jet} \sqrt{\gamma_{jet} R_{air} g (T_s)_{jet}} \tag{11}$$

$$\rho_{jet} = \left(\frac{(p_o)_{jet}}{R_{air} (T_o)_{jet}}\right) \left[\left(1 + \left(\frac{\gamma_{jet} - 1}{2}\right) M_{jet}^2\right)^{-\left(\frac{1}{\gamma_{jet} - 1}\right)}\right] \tag{12}$$

The jet ideal weight flow rate can be calculated as $(\dot{w}_{jet})_{ideal} = \rho_{jet} U_{jet} A_{exit}$, but is re-written as shown in Equation 13 to determine the maximum weight flow rate at $M_{jet} = 1$. The total ideal weight flow rate is calculated by summing the individual ideal weight flow rate values from each plenum as shown in Equation 14.

$$(\dot{w}_{jet})_{ideal} = M_{jet} \, A_{exit} \, (p_o)_{jet} \sqrt{\left(\frac{g \, \gamma_{jet}}{R_{air} \, (T_o)_{jet}}\right) \left[\left(1 + \left(\frac{\gamma_{jet} - 1}{2}\right) M_{jet}^2\right)^{-\left(\frac{\gamma_{jet} + 1}{\gamma_{jet} - 1}\right)}\right]} \qquad \text{for } M_{jet} < 1 \quad (13a)$$

$$(\dot{w}_{jet})_{ideal} = A_{exit} \, (p_o)_{jet} \sqrt{\left(\frac{g \, \gamma_{jet}}{R_{air} \, (T_o)_{jet}}\right) \left[\left(\frac{\gamma_{jet} + 1}{2}\right)^{-\left(\frac{\gamma_{jet} + 1}{\gamma_{jet} - 1}\right)}\right]} \qquad \text{for } M_{jet} = 1$$

$$(13b)$$

$$\left[(\dot{w}_{jet})_{ideal}\right]_{total} = \sum_{k=1}^{4} (\dot{w}_{jet})_{ideal}\big|_{k} \qquad (14)$$

The MCV system in the NTF air station provides a measure of the total weight flow rate through the model. The total measured weight flow rate $(\dot{w}_{MCV})$ is split among the four plenums using the ratio of the individual ideal weight flow rate to the total ideal weight flow rate as shown in Equation 15. Using the ideal weight flow rate ratio to split the measured total weight flow rate is better than using the slot exit area ratio because the area ratio is valid only when all of the plenums are set to the same NPR setting. There are cases when the plenums were tailored to operate at different NPR settings and these cases are handled correctly by using the ideal weight flow rate ratio.

$$(\dot{w}_{jet})_{meas} = \dot{w}_{MCV} \left(\frac{(\dot{w}_{jet})_{ideal}}{\left[(\dot{w}_{jet})_{ideal}\right]_{total}}\right) \qquad (15)$$

The nozzle discharge coefficient (C_{dis}) is calculated as the ratio of the measured weight flow rate to the ideal weight flow rate as shown in Equation 16. The discharge coefficient for each plenum is equal to the total discharge coefficient by design, because the measured total weight flow rate was split between the plenums using the ideal weight flow rate ratio.

$$(C_{dis})_{jet} = \frac{(\dot{w}_{jet})_{meas}}{(\dot{w}_{jet})_{ideal}} \qquad (16)$$

The momentum thrust from the blowing slot is calculated using the weight flow rate and the jet velocity at the slot exit. Since there are two values of weight flow rate, Equation 17 shows the momentum thrust calculated using the ideal weight flow rate with corresponding discharge coefficient and Equation 18 shows the momentum thrust calculated using the measured weight flow rate.

$$\left[(F_{mom})_{jet}\right]_{wideal} = \frac{(C_{dis})_{jet} \, (\dot{w}_{jet})_{ideal} \, U_{jet}}{g} \qquad (17)$$

$$\left[(F_{mom})_{jet}\right]_{wmeas} = \frac{(\dot{w}_{jet})_{meas} \, U_{jet}}{g} \qquad (18)$$

The momentum thrust is then non-dimensionalized by the freestream dynamic pressure and wing reference area to produce the momentum thrust coefficient (C_μ) as shown in Equations 19 and 20, corresponding to the ideal weight flow rate and measured weight flow rate respectively.

$$\left[(C_\mu)_{jet}\right]_{wideal} = \frac{\left[(F_{mom})_{jet}\right]_{wideal}}{q_\infty \, S_{ref}} \qquad (19)$$

$$\left[(C_\mu)_{jet}\right]_{wmeas} = \frac{\left[(F_{mom})_{jet}\right]_{wmeas}}{q_\infty \, S_{ref}} \qquad (20)$$

American Institute of Aeronautics and Astronautics

The pressure component of the total thrust from the blowing slot is calculated by applying the difference in pressure between the slot exit static pressure and the freestream static pressure (or back pressure in wind-off runs), across the slot exit area as shown in Equation 21.

$$(F_{pres})_{jet} = A_{exit} \ (p_{exit} - p_\infty) \tag{21}$$

Finally, the total thrust (momentum + pressure) is calculated in Equations 22 and 23, corresponding to the ideal weight flow rate and measured weight flow rate respectively. The total thrust is then non-dimensionalized by the freestream dynamic pressure and wing reference area to produce the total thrust coefficient (C_T) as shown in Equations 24 and 25.

$$\left[(F_{total})_{jet}\right]_{wideal} = \left[(F_{mom})_{jet}\right]_{wideal} + (F_{pres})_{jet} \tag{22}$$

$$\left[(F_{total})_{jet}\right]_{wmeas} = \left[(F_{mom})_{jet}\right]_{wmeas} + (F_{pres})_{jet} \tag{23}$$

$$\left[(C_T)_{jet}\right]_{wideal} = \frac{\left[(F_{total})_{jet}\right]_{wideal}}{q_\infty \ S_{ref}} \tag{24}$$

$$\left[(C_T)_{jet}\right]_{wmeas} = \frac{\left[(F_{total})_{jet}\right]_{wmeas}}{q_\infty \ S_{ref}} \tag{25}$$

2. Static Thrust Tare Results

During a thrust tare run for the FAST-MAC model with the tunnel fan not operating ($M_\infty = 0$), the four model valves are opened individually to set the NPR of each plenum to the desired level. The temperatures in the plenums are allowed to come to equilibrium and then a data point is acquired. This process is repeated for all desired NPR levels up to the maximum NPR level achievable before model safety limits are reached. From these runs, the static thrust from the blowing slot can be calculated. The focus of the paper is on the thrust tares with all plenums flowing to avoid the influences of single plenum interactions with unblown plenums.[20] Table 3 shows a listing of the thrust tares that were acquired during Test 213 for all flap configurations at various tunnel temperatures and back pressures. Note that there were a few runs where adjacent plenums were tailored and not set to the same NPR level. Also, there were a few runs acquired at a constant NPR while the model was moved through an angle of attack sweep.

In each of the plenums in the FAST-MAC model, the plenum area contracts to the slot exit area by a 6-to-1 ratio or a 12-to-1 ratio depending on the h/c configuration. The blowing slot is assumed to operate like a two-dimensional axisymmetric convergent nozzle (Figure 9). As the stagnation pressure in the plenum is increased and the ambient back pressure is held constant, the flow continues to accelerate in the plenum until $NPR_{critical}$ is reached and the

(a) Subsonic flow

(b) Choked flow

(c) Choked flow, underexpanded

Figure 9. Operation of a convergent nozzle at a constant ambient back pressure.

flow becomes choked at the slot exit. The static pressure at the slot exit is equal to the ambient back pressure until the flow chokes at the slot exit. Further increases in the stagnation pressure does not affect the local Mach number or velocity at the slot exit as it remains choked, however, the static pressure at the slot exit will increase linearly with the increased stagnation pressure to maintain the value of $NPR_{critical}$ at the slot exit. It is recognized that the blowing slot is not an axisymmetric nozzle and the wall-bounded jet complicates matters, but for the purposes of this thrust removal method, the blowing slot is treated as if it is exhausting into the ambient back pressure and not over the flap.

Table 3. Details of wind-off thrust tare runs (all plenums flowing) for the FAST-MAC model taken during NTF Test 213.

| Flap Angle, deg | Slot Design Constant | Thrust Tares Details (All Plenums Flowing) | | | | | |
		Adjacent Plenum States	Tunnel T_t , °F	Tunnel p_t , psi	NPR	α, deg	Run
0	$h/c = 0.0021$	Same NPR	-50	15	$1 - 2.6$	0	322
0	$h/c = 0.0021$	Same NPR	-50	27	$1 - 2.6$	0	305
0	$h/c = 0.0021$	Different NPR	-50	27	$1 - 2.6$	0	321
0	$h/c = 0.0021$	Same NPR	70	15	$1 - 2.6$	0	328
0	$h/c = 0.0021$	Same NPR	70	22	$1 - 2.6$	0	329
0	$h/c = 0.0021$	Different NPR	70	22	$1 - 2.6$	0	330, 376
30	$h/c = 0.0021$	Same NPR	-50	24	$1 - 2.8$	0	239
30	$h/c = 0.0021$	Same NPR	-50	47	$1 - 2.8$	0	248
30	$h/c = 0.0021$	Same NPR	-50	71	$1 - 2.8$	0	261
30	$h/c = 0.0021$	Same NPR	70	34	$1 - 2.8$	0	216
30	$h/c = 0.0021$	Same NPR	70	68	$1 - 2.8$	0	229
30	$h/c = 0.0021$	Same NPR	70	34	1.4	-20 − 28	217
30	$h/c = 0.0021$	Same NPR	70	68	1.4	-20 − 28	230
30	$h = 0.041$ in	Same NPR	70	34	$1 - 2.8$	0	292
30	$h = 0.041$ in	Same NPR	70	68	$1 - 2.8$	0	285
30	$h = 0.041$ in	Same NPR	70	68	1.4	-20 − 28	286
60	$h/c = 0.0021$	Same NPR	70	15	$1 - 3.2$	0	91
60	$h/c = 0.0021$	Same NPR	70	34	$1 - 3.2$	0	106
60	$h/c = 0.0021$	Same NPR	70	68	$1 - 3.2$	0	102
60	$h/c = 0.0032$	Same NPR	70	34	$1 - 3.2$	0	200
60	$h/c = 0.0032$	Same NPR	70	68	$1 - 3.2$	0	199

Therefore, it is expected that as the NPR is increased, the local exit pressure ratio NPR_{exit} also increases equally until $NPR_{critical}$ is reached and a choked condition at the slot exit is achieved. After this point, the local exit pressure ratio should remain the same value ($NPR_{exit} = NPR_{critical}$) even with further increases to NPR since the slot exit remains choked. One of the reasons for putting static pressure taps as close to the slot exit as possible (Figure 7) is to verify this expected behavior. Unfortunately, this behavior was not observed for all model configurations and all plenums using the measured data. Figure 10 shows NPR_{exit} plotted against NPR for all of the thrust tare runs acquired for the 0°, 30°, and 60° flap configurations. The four plots correspond to the four plenums and the plots show that NPR_{exit} flattens out for all of the thrust tare runs suggesting that the slot exit does achieve a choked condition for all configurations, but it doesn't always occur at $NPR_{critical}$ as expected. The stagnation pressures measured in the plenums are common to the equations for NPR and NPR_{exit} and the tunnel ambient back pressure was held constant throughout the thrust tare, therefore the unexpected behavior is caused by the non-uniformity of the static pressures measured at the slot exit. The data from the 0° cruise flap shows behavior closest to expectations, but all of the plenums do not exhibit the same behavior. For the 60° flap configuration, the measured exit static pressure was consistently lower than the ambient back pressure for $NPR \leq NPR_{critical}$ leading to the inflated values of NPR_{exit}. Possible explanations for the variability in the exit static pressure measurements include the difficulties in machining the pressure taps in the correct locations to line up with the slot exit and the difficulties of measuring the exit static pressure of a wall-bounded jet because the jet quickly accelerates over the Coandă surface.

The slot exit static pressure is needed to calculate the pressure thrust component of the total thrust, therefore the measured exit static pressure data was corrected to follow the expected trends. Specifically, the slot exit static pressure is set equal to the tunnel ambient back pressure ($p_{exit} = p_b$) up until a choked condition occurs at $NPR = NPR_{critical}$ and then from that point on, increasing the NPR causes the slot
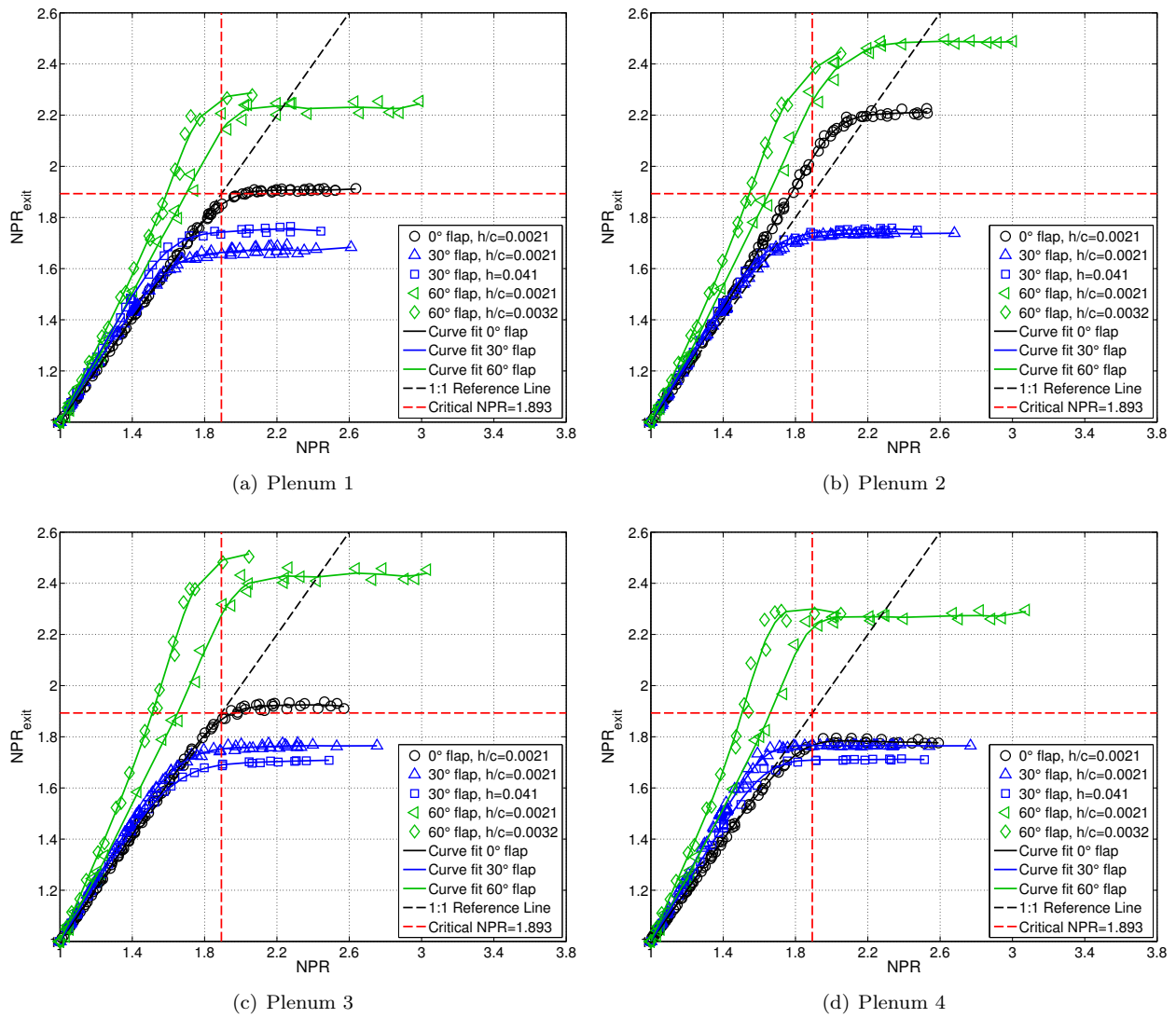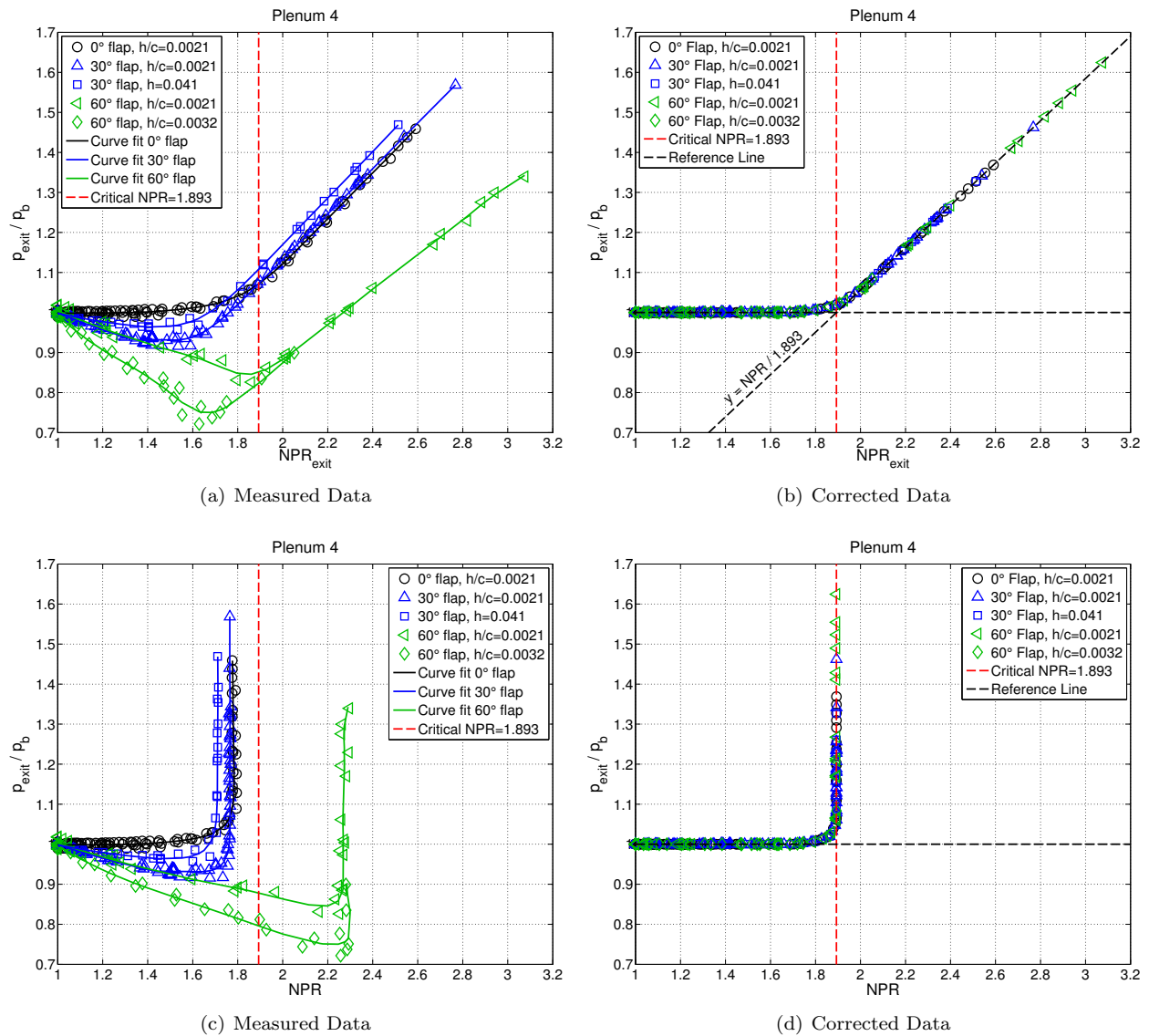
American Institute of Aeronautics and Astronautics

(a) Plenum 1

(b) Plenum 2

(c) Plenum 3

(d) Plenum 4

Figure 10. Comparison of NPR_{exit} and NPR for the four plenums in the FAST-MAC model.

exit static pressure to increase linearly with the plenum stagnation pressure to maintain the choked condition and maintain the local exit pressure ratio ($NPR_{exit} = NPR_{critical}$). The results of this correction are shown in Figure 11 for plenum #4 as an example. Notice that the corrected exit static pressure follows a slope equal to the value of $NPR_{critical}$, which forces NPR_{exit} to stay equal to $NPR_{critical}$ even for NPR values greater than $NPR_{critical}$. With this correction, the values calculated for the pressure thrust are consistent across all flap and slot height configurations.

The next step is to determine the weight flow rate through the blowing slot. Typically, the measured weight flow rate is lower than the calculated ideal weight flow rate due to losses incurred from real gas effects and nozzle deficiencies. This would lead to nozzle discharge coefficients or efficiency factors below 1 ($C_{dis} < 1$). Unfortunately, the data from the FAST-MAC thrust tares showed measured weight flow rates that were *higher* than the calculated ideal weight flow rate leading to discharge coefficients greater than 1, which are not realizable. In Figure 12, the weight flow rates are scaled by $p_b A_{exit}$ and plotted against NPR and the corresponding discharge coefficients are also shown. There is considerable scatter in the measured weight flow rate data, but the quoted uncertainties in the MCV weight flow rate measurements and the quoted uncertainties in the stagnation pressure measurements are not enough to account for the 5%-10% differences between the two weight flow rate values. The measurement of the slot exit areas could be the source of some error, but again are not enough to cover the 5%-10% differences either. Another explanation could be a leak in the system either before the model or at the model, but pre-test and post-test pressure

American Institute of Aeronautics and Astronautics

(a) Measured Data   (b) Corrected Data

(c) Measured Data   (d) Corrected Data

Figure 11. Corrections applied (b and d) to measured static pressure data (a and c) at slot exit relative to NPR **and** NPR_{exit}.

leaks of the entire flow control system did not show any appreciable leaks. The source of this weight flow rate discrepancy has not been uncovered and remains an open issue, therefore both sets of weight flow rate values are used in the calculation of the momentum thrust for comparison purposes. The ideal weight flow rate values assume a nozzle efficiency of unity ($C_{dis} = 1$) without further information to determine a better value.

Recall that the thrust tares were acquired at various back pressures for each of the flap and slot height configurations. This produced different values of the momentum thrust since the stagnation pressure in the plenums needed to be adjusted to achieve the same NPR value due to different back pressures. Also, each of the configurations had different values of the slot exit area, which also varies the amount of thrust generated. The momentum thrust values for all of these cases can be collapsed into a single curve using the "p_b method" by non-dimensionalizing the thrust by p_b and A_{exit} as shown in Equation 26. The same process can be applied to the pressure thrust and the total thrust as shown in Equations 27 and 28, respectively.

$$C_{F_{mom}} = \frac{F_{mom}}{p_b\, A_{exit}} \qquad (26) \qquad\qquad C_{F_{pres}} = \frac{F_{pres}}{p_b\, A_{exit}} \qquad (27) \qquad\qquad C_{F_{total}} = \frac{F_{total}}{p_b\, A_{exit}} \qquad (28)$$

American Institute of Aeronautics and Astronautics

(a) Scaled Weight Flow Rate $\left(\dfrac{\dot{w}}{p_b\,A_{exit}}\right)$

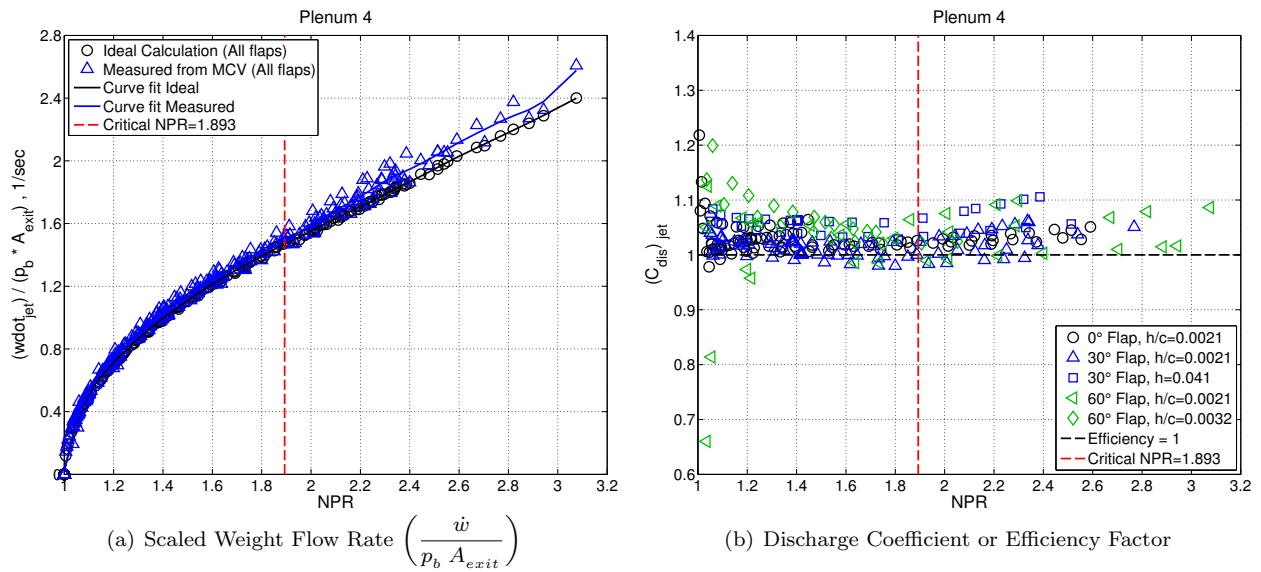(b) Discharge Coefficient or Efficiency Factor

Figure 12. Comparison of scaled ideal total weight flow rate to scaled measured total weight flow rate (a) and calculated discharge coefficients or efficiency factors (b).

The results are shown in Figure 13 for plenum #4 for the momentum thrust calculated using the ideal weight flow rate. It is clear that the various momentum thrust values at different back pressures for each flap configuration are collapsed into a single non-dimensional curve. Also, for comparison purposes, the non-dimensional momentum thrust using the measured weight flow rate is shown in Figure 14. The scatter in the non-dimensional momentum thrust in Figure 14(b) comes directly from the scatter in the measured weight flow rate data. The "p_b method" can also be applied to the corrected pressure thrust values and the total thrust (momentum + pressure) values as shown in Equations 28(b) and 28(c), respectively. Figure 15 shows the non-dimensional total thrust using both the ideal weight flow rate and measured weight flow rate and Figure 16 shows a comparison between the non-dimensional momentum thrust, the non-dimensional pressure thrust, and the non-dimensional total thrust.

(a) Momentum Thrust (F_{mom})

(b) Non-dimensional Momentum Thrust $\left(\dfrac{F_{mom}}{p_b\,A_{exit}}\right)$
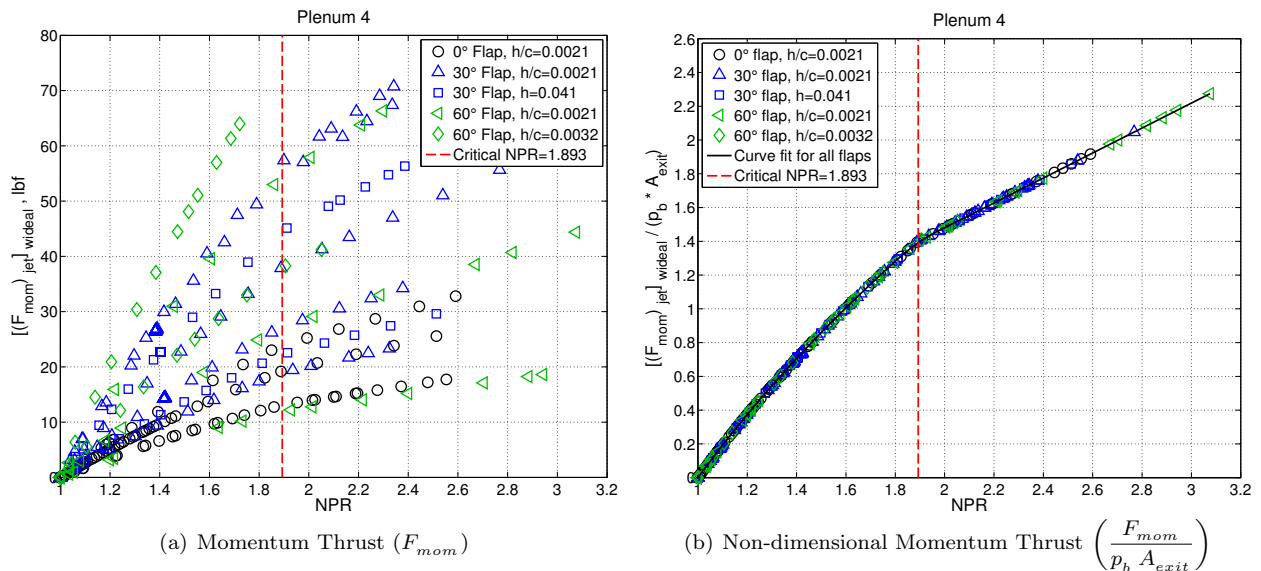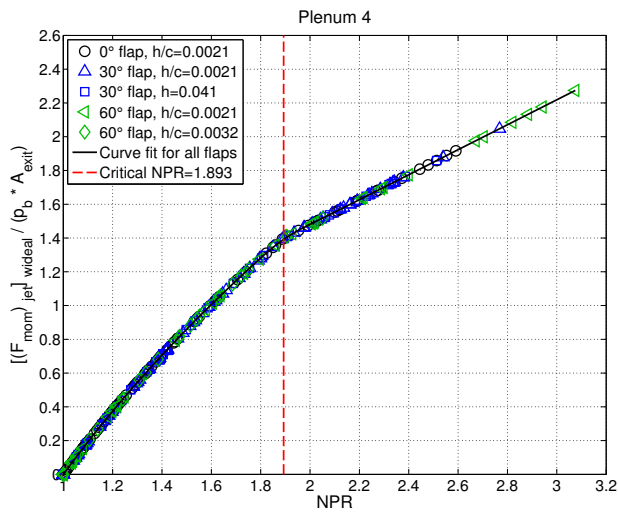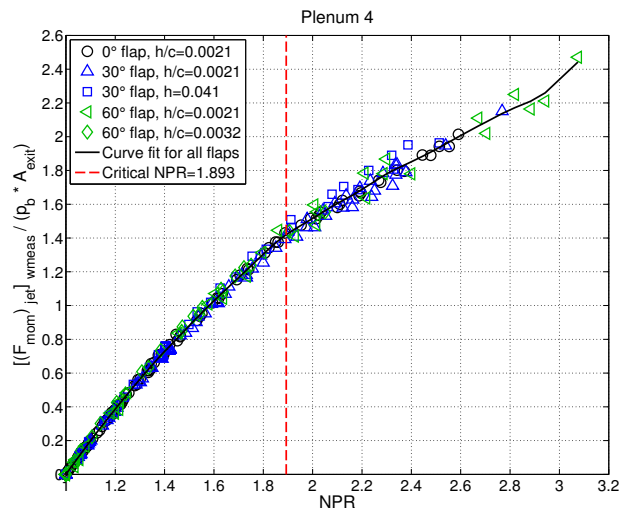
Figure 13. Calculated momentum thrust data using the ideal weight flow rate shown in (a) EU form at different ambient back pressures and (b) non-dimensional form.
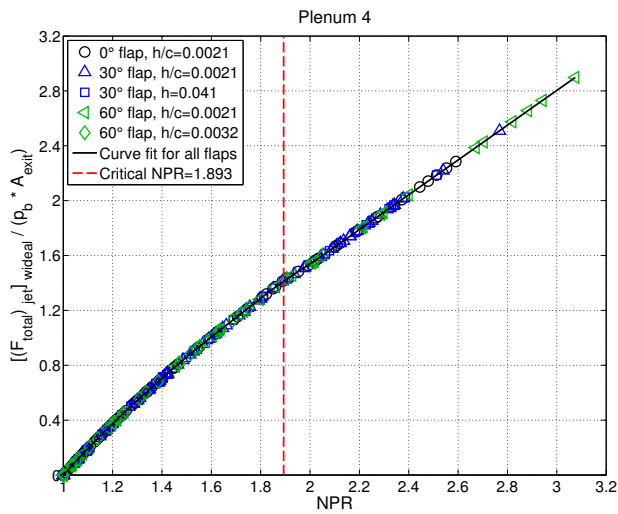
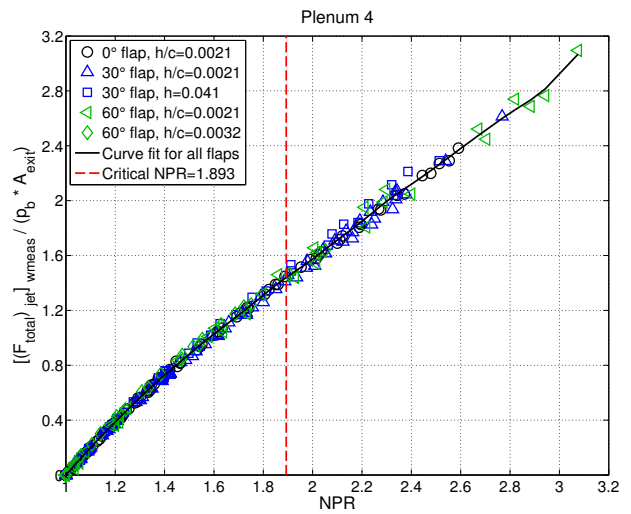(a) Using Ideal Weight Flow Rate

(b) Using Measured Weight Flow Rate

Figure 14.   Comparison of the calculated non-dimensional momentum thrust using (a) the ideal weight flow rate and (b) the measured weight flow rate.

(a) Using Ideal Weight Flow Rate

(b) Using Measured Weight Flow Rate

Figure 15.   Comparison of the calculated non-dimensional total thrust using (a) the ideal weight flow rate and (b) the measured weight flow rate.

American Institute of Aeronautics and Astronautics

(a) Using Ideal Weight Flow Rate

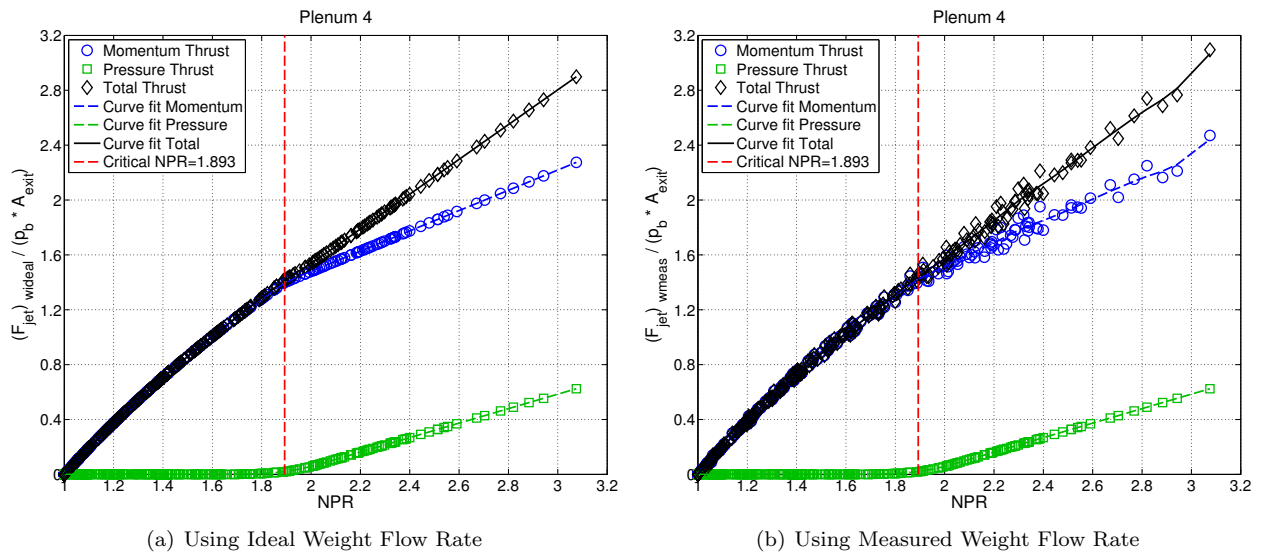(b) Using Measured Weight Flow Rate

Figure 16. Comparison of the calculated non-dimensional momentum thrust, non-dimensional pressure thrust, and non-dimensional total thrust using (a) the ideal weight flow rate and (b) the measured weight flow rate.

At this point, a decision needed to be made regarding which of the total thrust curves were going to be used for the thrust removal application. The total thrust curves using the ideal weight flow rate with $C_{dis} = 1$ were chosen for several reasons. The ideal weight flow rate values used measurements very close to the blowing slot giving confidence that the correct stagnation quantities were measured. In contrast, the MCV measured the weight flow rate outside of the tunnel at the beginning of the HPA supply line. Secondly, the MCV weight flow rate measurements displayed more scatter than was expected or desired. Finally, the MCV systems have not been calibrated properly since the mid 1990's and it is conceivable that after extensive use, the calibration may have shifted. There are plans to re-calibrate the MCV systems at a dedicated calibration facility, which will determine whether the existing calibration is valid.

3. Comparison to Balance Data

It was noted earlier that because the blowing jet was directed over the flap, the balance force and moment measurements during a thrust tare would not be able to distinguish between the static thrust effect and the aerodynamic Coandă effect, and would measure the combined effect. This is the main reason why the balance data was not chosen to be used for the thrust removal methodology. Additionally, the thrust loads from the blowing slot are relatively small and amounted to less than 11% of the balance capacity in axial force and less than 2% in normal force. However, the balance data can still be used as a sanity check against the calculated thrust values to make sure the thrust values are reasonable. The calculated total thrust values can be compared to the resultant thrust measured by the balance, where the resultant thrust is the root-sum-square of the measured balance forces as shown in Equation 1. Note that the NTF-117S balance does not possess a side force measurement, therefore a component is missing in this resultant. However, even with this missing component, the balance resultant thrust compares well to the calculated total thrust. Figure 17(a) shows a comparison between the non-dimensional total thrust and the non-dimensional balance resultant thrust for the 0° cruise flap thrust tares. Figure 17(b) shows a comparison of the non-dimensional yawing moment induced by the calculated total thrust and the non-dimensional yawing moment measured by the balance. The calculated total thrust from each plenum was resolved into the x and y directions, then applied at the middle of each plenum to produce a yawing moment at the balance moment center (BMC) in order to compare to the balance measurement of yawing moment. Since the curves in both cases compare well with each other, it shows that the calculated total thrust is reasonable.

American Institute of Aeronautics and Astronautics

(a) Non-dimensional Resultant Thrust   (b) Non-dimensional Yawing Moment
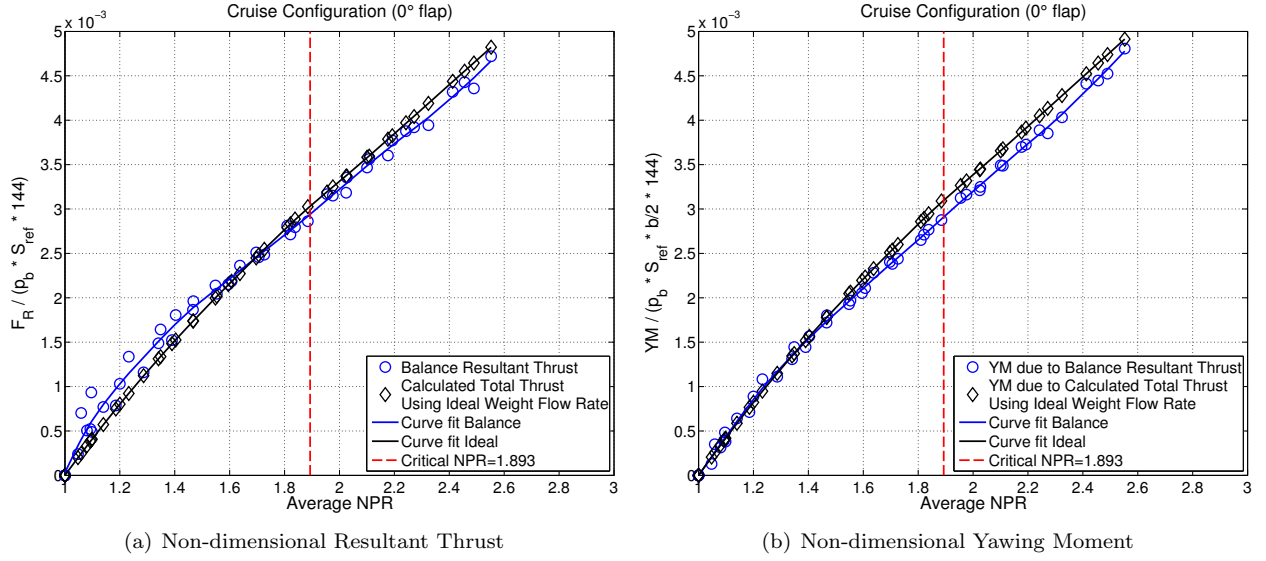
Figure 17. Comparison between the balance data and the calculated total thrust using the ideal weight flow rate for (a) the non-dimensional resultant thrust and (b) the non-dimensional yawing moment for the 0° cruise flap thrust tares.

4. Application of Thrust Removal

The non-dimensional total thrust curves using the ideal weight flow rate were determined for each plenum. These curves are used to determine the total thrust out of the blowing slot at wind-on conditions based on NPR, the slot exit areas, and the freestream static pressure. Note that the curves are not a function of angle of attack because the static thrust vectors always reside on the model axis. However, since the thrust vector is angled with respect to the model $x - y$ plane and $x - z$ plane, the total thrust must be resolved along the x, y, and z axes. Figure 18 shows the thrust vector pitch angle θ_{thrust} and yaw angle ψ_{thrust} for each plenum and the angles are listed in Table 4. The total thrust is resolved along the x, y, and z axes by performing pitch and yaw Euler rotations. The resolved thrust components are shown in Equation 29. Note that the negative signs are the result of mapping the standard right-hand Euler axes to the aircraft model axes definition.

$$(F_{total})x = F_{total} \cos\theta_{thrust} \cos\psi_{thrust} \tag{29a}$$

$$(F_{total})y = -F_{total} \cos\theta_{thrust} \sin\psi_{thrust} \tag{29b}$$

$$(F_{total})z = -F_{total} \sin\theta_{thrust} \tag{29c}$$

Table 4. Thrust vector angles in the aircraft model axes.

Plenum	θ_{thrust}	ψ_{thrust}
1	7.1°	-16.1°
2	7.2°	-16.1°
3	7.7°	-16.1°
4	8.0°	-16.1°

American Institute of Aeronautics and Astronautics

(a) Thrust Vector Pitch Angle
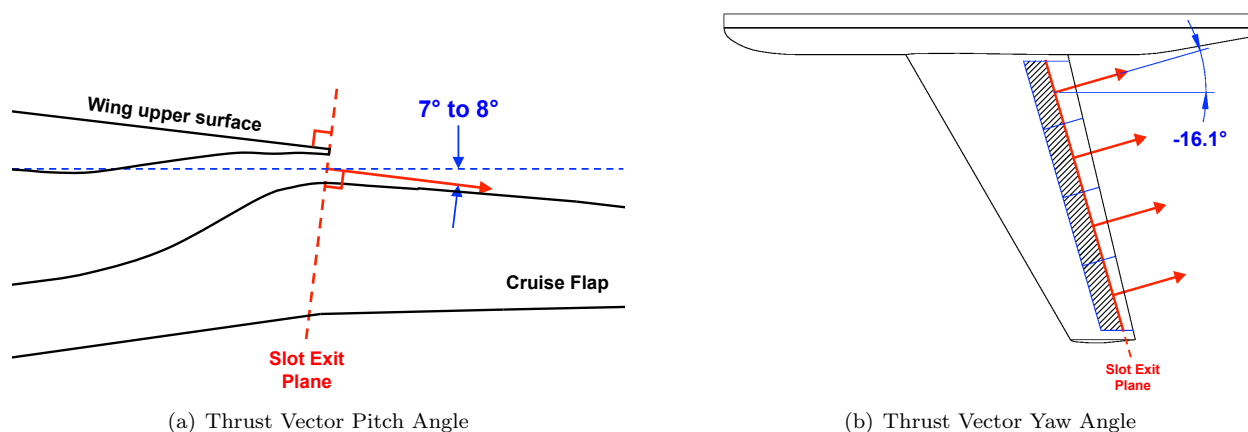

(b) Thrust Vector Yaw Angle

Figure 18. Blowing slot thrust vector (a) pitch angle and (b) yaw angle in the aircraft model axes.

The total thrust from each plenum is assumed to act at the center of each plenum span. Figure 19 shows the distances from each of the thrust vectors to the moment reference center (MRC) in both the x and y axes and also shows the distances from the BMC to the MRC. These values are listed in Table 5. The distances from the thrust vectors to the MRC are used to determine the moments generated at the MRC due to the static thrust. These moments due to the static thrust are then removed from the wind-on data.
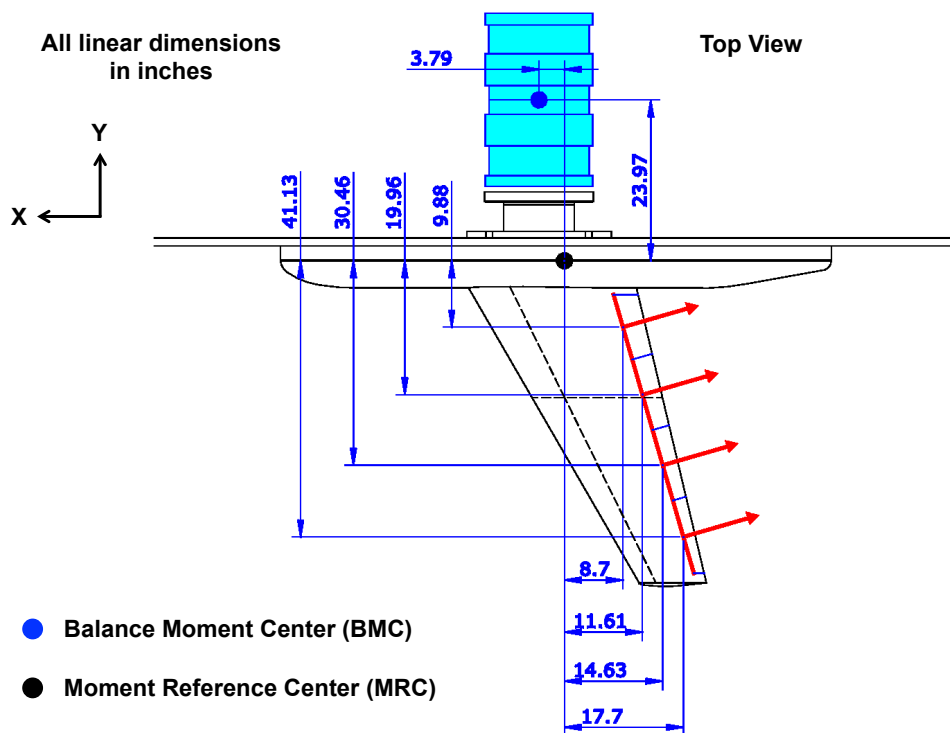

Figure 19. Test setup for FAST-MAC model showing locations of the BMC, MRC and thrust vectors from each model plenum.

American Institute of Aeronautics and Astronautics

Table 5. Transfer distances (model-scale) to the MRC location from the BMC and from the thrust vectors.

Component	BMC to MRC, in	Thrust Vector to MRC, in			
		Plenum 1	Plenum 2	Plenum 3	Plenum 4
$\overline{x}$	-3.79	17.70	14.63	11.61	8.70
$\overline{y}$	-23.97	41.13	30.46	19.96	9.88
$\overline{z}$	0	0	0	0	0

The procedure for the application of the thrust removal methodology onto the wind-on balance force and moment measurements is listed below.

<u>For each wind-on data point:</u>

1. Use the $NPR|_{1-4}$ values for each plenum to lookup the non-dimensional total thrust value $\left(C_{F_{total}} \Big|_{1-4} \right)$ from the thrust tares using linear interpolation.

2. Multiply the $C_{F_{total}} \Big|_{1-4}$ lookup value by the freestream static pressure and the slot exit area for each plenum. This produces the dimensional total thrust $\left(F_{total}|_{1-4} \right)$ from each plenum at the wind-on condition.

   - $F_{total}|_{1-4} = C_{F_{total}} \Big|_{1-4} \left(p_{\infty} \ A_{exit}|_{1-4} \right)$

3. Resolve the total thrust from each plenum into the x, y, and z axes using Equation 29. Then, sum the resolved thrust components from each plenum to produce the total AF, SF, and NF due to thrust. Note the negative sign because the thrust produces an equal force in the opposite direction. Also, determine the RM, PM, and YM generated at the MRC by the resolved thrust components from each plenum.

   - $AF_{thrust} = \sum\limits_{k=1}^{4} \left[-(F_{total})x|_{k} \right]$

   - $SF_{thrust} = \sum\limits_{k=1}^{4} \left[-(F_{total})y|_{k} \right]$

   - $NF_{thrust} = \sum\limits_{k=1}^{4} \left[-(F_{total})z|_{k} \right]$

   - $RM_{thrust} = \sum\limits_{k=1}^{4} \left[-(F_{total})z|_{k} \left(\overline{y}_{thrust}|_{k} \right) + (F_{total})y|_{k} \left(\overline{z}_{thrust}|_{k} \right) \right]$

   - $PM_{thrust} = \sum\limits_{k=1}^{4} \left[(F_{total})z|_{k} \left(\overline{x}_{thrust}|_{k} \right) + (F_{total})x|_{k} \left(\overline{z}_{thrust}|_{k} \right) \right]$

   - $YM_{thrust} = \sum\limits_{k=1}^{4} \left[(F_{total})y|_{k} \left(\overline{x}_{thrust}|_{k} \right) + (F_{total})x|_{k} \left(\overline{y}_{thrust}|_{k} \right) \right]$

4. Convert the forces and moments due to thrust to coefficient form.

   - $(C_A)_{thrust} = \left(\dfrac{AF_{thrust}}{q_{\infty} \ S_{ref}} \right)$

   - $(C_Y)_{thrust} = \left(\dfrac{SF_{thrust}}{q_{\infty} \ S_{ref}} \right)$

   - $(C_N)_{thrust} = \left(\dfrac{NF_{thrust}}{q_{\infty} \ S_{ref}} \right)$

American Institute of Aeronautics and Astronautics

- $(C_l)_{thrust} = \left(\dfrac{RM_{thrust}}{q_\infty \, S_{ref} \, (b/2)} \right)$

- $(C_m)_{thrust} = \left(\dfrac{PM_{thrust}}{q_\infty \, S_{ref} \, \bar{c}} \right)$

- $(C_n)_{thrust} = \left(\dfrac{YM_{thrust}}{q_\infty \, S_{ref} \, (b/2)} \right)$

- $(C_D)_{thrust} = [(C_A)_{thrust} \cos \alpha + (C_N)_{thrust} \sin \alpha]$

- $(C_L)_{thrust} = [(C_N)_{thrust} \cos \alpha - (C_A)_{thrust} \sin \alpha]$

5. Subtract the force and moment coefficients due to thrust from the wind-on force and moment coefficients to obtain the thrust-removed quantities.

- $(C_A)_{TR} = C_A - (C_A)_{thrust}$

- $(C_Y)_{TR} = C_Y - (C_Y)_{thrust}$

- $(C_N)_{TR} = C_N - (C_N)_{thrust}$

- $(C_l)_{TR} = C_l - (C_l)_{thrust}$

- $(C_m)_{TR} = C_m - (C_m)_{thrust}$

- $(C_n)_{TR} = C_n - (C_n)_{thrust}$

- $(C_D)_{TR} = C_D - (C_D)_{thrust}$

- $(C_L)_{TR} = C_L - (C_L)_{thrust}$

American Institute of Aeronautics and Astronautics

IV. Results

During the transonic portion of Test 213, the test focused on Mach numbers from 0.85 to 0.88 at chord Reynolds numbers of 10, 15, and 30 million. The tunnel stagnation temperature for the experiment was -50°F for cryogenic mode operations to reach the highest Reynolds numbers and 120°F in air mode operations. Data were acquired at angles of attack between -6° and +6° and the circulation control blowing varied between NPR values of 1.0 to 2.5 and C_μ values between 0 and 0.008.

Analysis of wing surface pressures for the 0° flap cruise configuration data from Test 213 showed encouraging results suggesting the potential for cruise drag reduction as a consequence of the blowing.[19] The thrust removal methodology laid out in Section III was applied to the wind-on balance data for the 0° flap cruise configuration to see if the drag reduction was realized or if the opposite occurred, i.e. the blowing induced additional drag to the configuration. Figure 20 shows a comparison between the uncorrected balance data and the thrust-removed corrected data for both lift and drag coefficient at $M_\infty = 0.85$ and $30\mathrm{x}10^6$ chord Reynolds number. This verified that the process produced reasonable thrust values and the corrections were applied in the proper direction.

(a) Uncorrected Data
(b) Thrust-removed Corrected Data
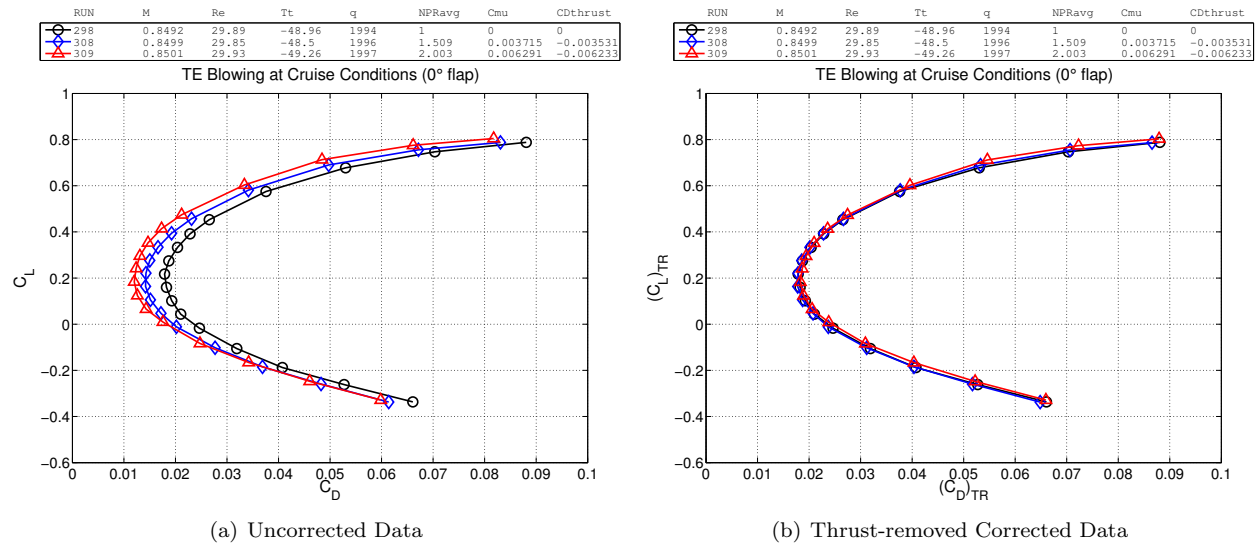
Figure 20. Comparison between (a) uncorrected data and (b) thrust-removed corrected data at $M_\infty = 0.85$ and 30 million Re.

Figure 21 shows the thrust-removed corrected lift coefficient and powered lift increment (ΔC_L) data for $M_\infty = 0.85$ and $M_\infty = 0.88$ at $30\mathrm{x}10^6$ chord Reynolds number. The data at $M_\infty = 0.85$ represents the effect of the circulation control blowing when the flow over the wing is fully attached since this is the design Mach number of the wing. The blowing provided a noticeable increase in the lift coefficient across the angle of attack range, corroborating the surface pressure analysis that showed the shockwave was moved aft without changing the shock strength. The data at $M_\infty = 0.88$ represents an off-design condition for the wing, but the data also showed an increase in the lift coefficient. For both Mach numbers, the powered lift increments are mostly greater than the balance repeatability levels for C_L.

To investigate whether the circulation control blowing provided a drag reduction, the thrust-removed data were evaluated at a constant $C_L = 0.5$, which is the design lift coefficient of the un-blown wing. Since the blowing provided a lift increase, each of the data curves were linearly interpolated as a function of C_L^2. The drag coefficients corresponding to $C_L = 0.5$ were determined from this interpolation. These values were then compared to the unpowered data to determine a drag increment due to the induced effect of the circulation control blowing. Figure 22 shows the results of this simple analysis at $M_\infty = 0.85$ and $M_\infty = 0.88$ at $30\mathrm{x}10^6$ chord Reynolds number. The $M_\infty = 0.85$ thrust-removed data at an average $NPR = 2.0$ and a $C_\mu = 0.0063$ showed a 7 count reduction in the drag coefficient at $C_L = 0.5$ from the unpowered baseline data. Even more impressive is the thrust-removed data at $M_\infty = 0.88$ at an average $NPR = 1.78$ and a $C_\mu = 0.0050$, which showed a 25 count reduction in the drag coefficient at $C_L = 0.5$ from the unpowered baseline data. At $M_\infty = 0.88$, the un-blown wing experiences significant shock-induced flow separation and

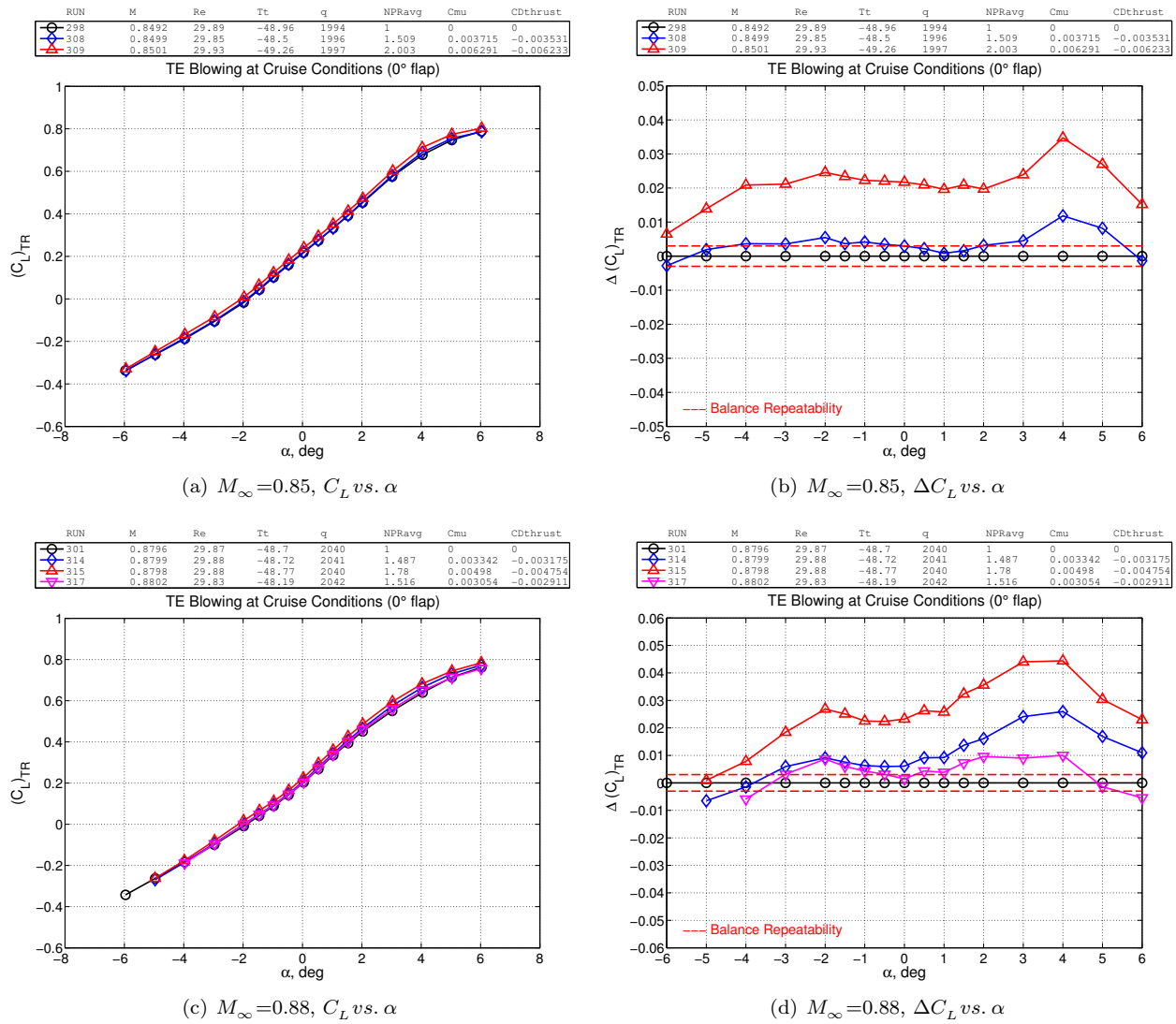American Institute of Aeronautics and Astronautics

(a) M_∞=0.85, C_L vs. α

(b) M_∞=0.85, ΔC_L vs. α

RUN	M	Re	Tt	q	NPRavg	Cmu	CDthrust
301	0.8796	29.87	-48.7	2040	1	0	0
314	0.8799	29.88	-48.72	2041	1.487	0.003342	-0.003175
315	0.8798	29.88	-48.77	2040	1.78	0.00498	-0.004754
317	0.8802	29.83	-48.19	2042	1.516	0.003054	-0.002911

(c) M_∞=0.88, C_L vs. α

(d) M_∞=0.88, ΔC_L vs. α

Figure 21. Thrust-removed corrected lift coefficient data and powered lift increments at 30 million Re for $M_\infty = 0.85$ and $M_\infty = 0.88$.

the blowing helps to re-attach the flow.[19]

While the magnitude of these drag reduction numbers seem significant, the reality is tempered by the fact that the balance system calibration accuracy at these conditions is ±6 counts and the balance data repeatability level for the cruise data was shown to be ±10 counts.[19] The drag increment was calculated as described above for constant lift coefficients from -0.4 to 0.8 and the results are shown in Figure 23. The ±10 counts data repeatability uncertainty is shown on the plots for reference. At $M_\infty = 0.85$, many of the calculated drag increments are within the band of the data repeatability uncertainty, meaning that the balance cannot resolve the drag increments at that condition. However, for lift coefficients above the design lift coefficient, there is a measurable drag reduction outside of the balance repeatability level. This suggests that with blowing, the wing may perform better and thus cruise at a higher lift coefficient. The wing was designed without blowing and perhaps a better design could be achieved by including blowing in the design process. The calculated drag increments at $M_\infty = 0.88$ showed similar results, but for the higher lift coefficients, significant drag reduction values were measured.
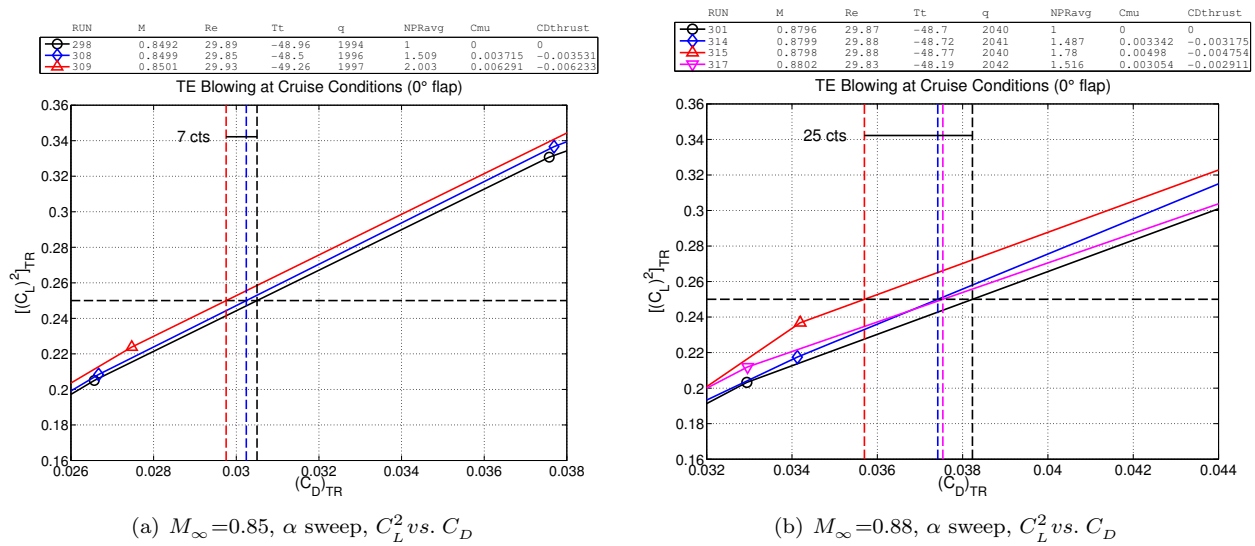
RUN	M	Re	Tt	q	NPRavg	Cmu	CDthrust
298	0.8492	29.89	-48.96	1994	1	0	0
308	0.8499	29.85	-48.5	1996	1.509	0.003715	-0.003531
309	0.8501	29.93	-49.26	1997	2.003	0.006291	-0.006233

RUN	M	Re	Tt	q	NPRavg	Cmu	CDthrust
301	0.8796	29.87	-48.7	2040	1	0	0
314	0.8799	29.88	-48.72	2041	1.487	0.003342	-0.003175
315	0.8798	29.88	-48.77	2040	1.78	0.00498	-0.004754
317	0.8802	29.83	-48.19	2042	1.516	0.003054	-0.002911

(a) $M_\infty = 0.85$, α sweep, C_L^2 vs. C_D

(b) $M_\infty = 0.88$, α sweep, C_L^2 vs. C_D

Figure 22. Thrust-removed drag increments at $C_L = 0.5$ due to the induced effect of the circulation control blowing at 30 million Re for $M_\infty = 0.85$ and $M_\infty = 0.88$.

RUN	M	Re	Tt	q	NPRavg	Cmu	CDthrust
298	0.8492	29.89	-48.96	1994	1	0	0
308	0.8499	29.85	-48.5	1996	1.509	0.003715	-0.003531
309	0.8501	29.93	-49.26	1997	2.003	0.006291	-0.006233

RUN	M	Re	Tt	q	NPRavg	Cmu	CDthrust
301	0.8796	29.87	-48.7	2040	1	0	0
314	0.8799	29.88	-48.72	2041	1.487	0.003342	-0.003175
315	0.8798	29.88	-48.77	2040	1.78	0.00498	-0.004754
317	0.8802	29.83	-48.19	2042	1.516	0.003054	-0.002911

(a) $M_\infty = 0.85$, α sweep, ΔC_D vs. C_L

(b) $M_\infty = 0.88$, α sweep, ΔC_D vs. C_L

Figure 23. Thrust-removed drag increments at constant lift coefficients at 30 million Re for $M_\infty = 0.85$ and $M_\infty = 0.88$.

A few NPR sweep runs at a constant $3°$ angle of attack corresponding to roughly $C_L = 0.6$ were acquired at transonic conditions at various Mach and chord Reynolds numbers. Two examples are shown in Figure 24. An unpowered data point was first acquired, then data points at increasing NPR and C_μ values were acquired. At $M_\infty = 0.85$, blowing at low NPR spoiled the lift on the configuration until about $NPR = 1.5$ when the lift coefficient recovered to the same level as the unpowered data point. However, at this blowing condition, the drag coefficient was reduced by 18 counts. At $M_\infty = 0.88$, it didn't take much blowing to recover to the same lift coefficient as the unpowered point. At about $NPR = 1.2$, the lift coefficient recovered, but with a 25 count reduction in drag coefficient.

Finally, the thrust-removed drag increments at $C_L = 0.5$ for several Reynolds numbers were calculated to see the effect of Reynolds number as this was one of the main reasons for testing at the NTF. The dynamic pressure at each of the Reynolds number conditions were not held constant, therefore, there are aeroelastic effects in addition to Reynolds number effects in the following results. This is shown in Figure 25 for $M_\infty = 0.85$ and $M_\infty = 0.88$. The ± 10 counts data repeatability uncertainty is again shown on the

plots for reference. At $M_\infty = 0.85$, the potential drag reduction as a consequence of the blowing seems to dissipate with increased Reynolds number irregardless of the blowing rate. At $M_\infty = 0.88$, the effect of Reynolds number is not as prevalent when compared to the effect of blowing rate. For the highest blowing rate of $NPR = 1.75$ at $M_\infty = 0.88$, the drag reduction shown is well outside of the balance repeatability level and should be considered a valid result.
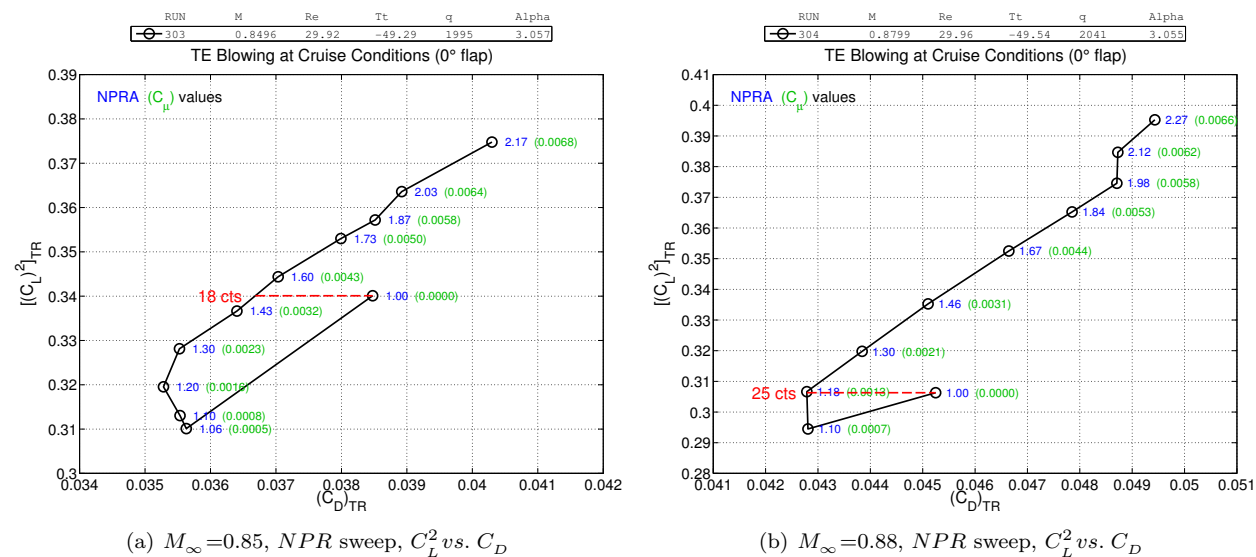

(a) M_∞=0.85, NPR sweep, C_L^2 vs. C_D

(b) M_∞=0.88, NPR sweep, C_L^2 vs. C_D

Figure 24. Thrust-removed NPR sweeps at constant $3°$ angle of attack at 30 million Re for M_∞=0.85 and M_∞=0.88. Average NPR values shown in blue and C_μ values shown in green for each data point.

(a) ΔC_D vs. Re

(b) ΔC_D vs. q_∞
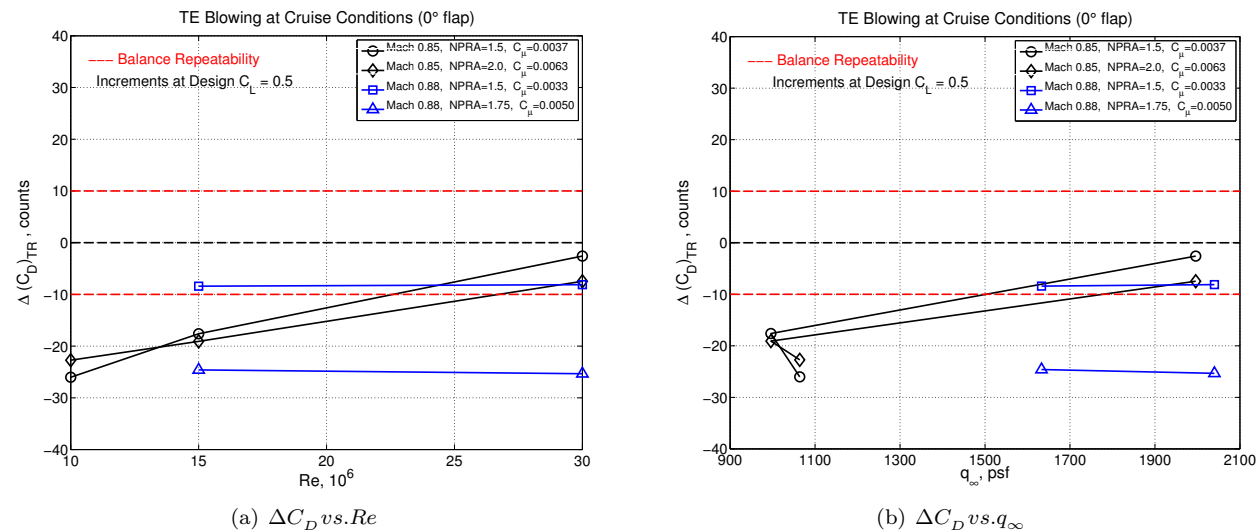
Figure 25. Interpolated effect of (a) Reynolds number and (b) dynamic pressure on the thrust-removed drag increments at $C_L = 0.5$ for M_∞=0.85 and M_∞=0.88.

Recent improvements[29] to the SMSS and NTF-117S balance have been designed to decrease the data repeatability uncertainty numbers so that a more accurate drag increment due to circulation control blowing can be measured. The results in this paper show that at some conditions, there is indeed a drag reduction benefit as a result of the blowing. The upcoming third test entry of the FAST-MAC model will test the improvements to the SMSS and NTF-117S balance and will also attempt to repeat the results gathered from Test 213. Furthermore, CFD studies on the FAST-MAC model are continuing and will provide a comparison to the wind-tunnel results.

V. Concluding Remarks

The focus of this paper has been on the development of the thrust removal methodology for the FAST-MAC circulation control model that was tested at the National Transonic Facility. Several options were considered for the thrust removal methodology as guidance was provided by typical methods used in historical propulsion and flow control simulation experiments. The chosen thrust removal method applied to the FAST-MAC experiments uses the measured stagnation quantities in each of the FAST-MAC plenums to calculate the thrust at the slot exit assuming the plenums operate like convergent nozzles and the jet expands adiabatically to the freestream static pressure. The calculated thrust from each plenum is then resolved into its x, y, and z components and summed to produce the final thrust quantities, which are used to correct the wind-on balance data.

A preliminary analysis of the thrust-removed corrected data shows potential drag reduction at the design lift coefficient ($C_L = 0.5$) of 8 counts at $M_\infty = 0.85$ and 27 counts at $M_\infty = 0.88$, both at 30 million Reynolds number based on mean chord. The balance system calibration uncertainty and the data repeatability level for the cruise data are on the order of ±10 counts, which makes it difficult to accept any drag reduction numbers below this value. However, at $M_\infty = 0.85$ at lift coefficients above the design, the drag reduction values were outside of the balance repeatability level, suggesting that a drag reduction benefit was realized at these higher lift coefficients. At $M_\infty = 0.88$, the blowing definitely provides a drag reduction benefit at the design lift coefficient and above, as many of the drag reduction numbers are more than two times larger than the uncertainty range. On-going CFD studies on the FAST-MAC model will help further the understanding of the flow physics related to the circulation control blowing at transonic conditions and will provide a comparison to the wind tunnel results.

Recent improvements to the SMSS and NTF-117S balance have been designed to decrease the uncertainty numbers so that a more accurate drag increment due to circulation control blowing can be measured in the upcoming third test entry of the FAST-MAC model. Furthermore, there are plans to build new calibration hardware to replace the flap with a nozzle to calibrate the thrust in each flow path. This will allow the balance data to be used to measure the pure static thrust effects during a wind-off thrust tare.

Acknowledgements

References

[1]Zeune, C. H., "An Overview of the Air Force's Speed Agile Concept Demonstration Program," AIAA Paper 2013-1097, AIAA, January 2013.

[2]Barberie, F. J., Wick, A. T., Hooker, J. R., and Zeune, C. H., "Low Speed Powered Lift Testing of a Transonic Cruise Efficient STOL Military Transport," AIAA Paper 2013-1099, AIAA, January 2013.

[3]Hooker, J. R., Wick, A. T., Zeune, C. H., Jones, G. S., and Milholen-II, W. E., "Design and Transonic Wind Tunnel Testing of a Cruise Efficient STOL Military Transport," AIAA Paper 2013-1100, AIAA, January 2013.

[4]Harrison, N. A., Vassberg, J. C., DeHaan, M. A., and Gea, L.-M., "The Design and Test of a Swept Wing Upper Surface Blowing (USB) Concept," AIAA Paper 2013-1102, AIAA, January 2013.

[5]Collins, S. W., Westra, B. W., Lin, J. C., Jones, G. S., and Zeune, C. H., "Wind Tunnel Testing of Powered Lift, All-Wing STOL Model," RAeS 566-5A3, Royal Aeronautical Society, London, July 2008.

[6]Jameson, K. K., Marshall, D. D., Ehrmann, R., Lichtwardt, J. A., Paciano, E., Englar, R. J., and Horne, W. C., "Cal Poly's AMELIA 10 Foot Span Hybrid Wing-Body Low Noise CESTOL Aircraft Wind Tunnel Test and Experimental Results Overview," AIAA Paper 2013-0974, AIAA, January 2013.

[7]Jones, G. S., Lin, J. C., Allan, B. G., Milholen-II, W. E., Rumsey, C. L., and Swanson, R. C., "Overview of CFD

American Institute of Aeronautics and Astronautics

Validation Experiments for Circulation Control Applications at NASA," RAeS 566-8A1, Royal Aeronautical Society, London, July 2008.

[8]Wick, A. T., Hooker, J. R., Barberie, F. J., and Zeune, C. H., "Powered Lift CFD Predictions of a Transonic Cruising STOL Military Transport," AIAA Paper 2013-1098, AIAA, January 2013.

[9]Marshall, D. D., Lichtwardt, J. A., Pham, J., Blessing, B., and Storm, T. M., "Summary of the Aerodynamic Modeling Efforts for AMELIA," AIAA Paper 2013-0973, AIAA, January 2013.

[10]Englar, R. J., Jones, G. S., Allan, B. G., and Lin, J. C., "2-D Circulation Control Airfoil Benchmark Experiments Intended for CFD Code Validation," AIAA Paper 2009-902, AIAA, January 2009.

[11]Pfingsten, K. C. and Radespiel, R., "Experimental and Numerical Investigation of a Circulation Control Airfoil," AIAA Paper 2009-533, AIAA, January 2009.

[12]Swanson, R. C., Rumsey, C. L., and Anders, S. G., "Progress Towards Computational Method for Circulation Control Airfoils," AIAA Paper 2005-89, AIAA, January 2005.

[13]Rogers, E. O. and Donnelly, M. J., "Characteristics of a Dual-Slotted Circulation Control Wing of Low Aspect Ratio Intended for Naval Hydrodynamic Applications," AIAA Paper 2004-1244, AIAA, January 2004.

[14]Jones, G. S., Viken, S. A., Washburn, A. E., Jenkins, L. N., and Cagle, C. M., "An Active Flow Circulation Controlled Flap Concept for General Aviation Aircraft Applications," AIAA Paper 2002-3157, AIAA, June 2002.

[15]Alexander, M. G., Anders, S. G., Johnson, S. K., Florance, J. P., and Keller, D. F., "Trailing Edge Blowing on a Two-Dimensional Six-Percent Thick Elliptical Circulation Control Airfoil Up to Transonic Conditions," NASA TM 2005-213545, NASA Langley Research Center, March 2005.

[16]Milholen-II, W. E., Jones, G. S., Chan, D. T., and Goodliff, S. L., "High-Reynolds Number Circulation Control Testing in the National Transonic Facility (Invited)," AIAA Paper 2012-0103, AIAA, January 2012.

[17]Englar, R. J., "Two-Dimensional Transonic Wind Tunnel Tests of Three 15-Percent-Thick Circulation Control Airfoils," Technical Note AL-182, AD 882-075, Naval Ship Research and Development Center, December 1970.

[18]Schlecht, R. and Anders, S. G., "Parametric Evaluation of Thin, Transonic Circulation Control Airfoils," AIAA Paper 2007-272, AIAA, January 2007.

[19]Milholen-II, W. E., Jones, G. S., Chan, D. T., Goodliff, S. L., Anders, S. G., Melton, L. P., Carter, M. B., Allan, B. G., and Capone, F. J., "Enhancements to the FAST-MAC Circulation Control Model and Recent High-Reynolds Number Testing in the National Transonic Facility," AIAA Paper 2013-2794, AIAA, June 2013.

[20]Jones, G. S., Milholen-II, W. E., Chan, D. T., Allan, B., Goodliff, S. L., Melton, L., Anders, S. G., Carter, M., and Capone, F., "Development of the Circulation Control Flow Scheme used in the NTF Semi-Span FAST-MAC Model," AIAA Paper 2013-3048, AIAA, June 2013.

[21]Wahls, R. A., "The National Transonic Facility: A Research Retrospective (Invited)," AIAA Paper 2001-754, AIAA, January 2001.

[22]Milholen-II, W. E., Jones, G. S., and Cagle, C. M., "NASA High-Reynolds Number Circulation Control Research - Overview of CFD and Planned Experiments (Invited)," AIAA Paper 2010-344, AIAA, January 2010.

[23]Englar, R. J., Smith, M. J., Kelley, S. M., and Rover-III, R. C., "Application of Circulation Control Technology to Advanced Subsonic Transport Aircraft, Part I: Airfoil Development," *Journal of Aircraft*, Vol. 31, No. 5, Sept-Oct 1994, pp. 1160–1168.

[24]Gatlin, G. M., Parker, P. A., and Owens, L. R., "Development of a Semi-Span Test Capability at the National Transonic Facility," AIAA Paper 2001-0759, AIAA, January 2001.

[25]Berrier, B. L., Leavitt, L. D., and Bangert, L. S., "Operating Characteristics of the Multiple Critical Venturi System and Secondary Calibration Nozzles Used for Weight-Flow Measurements in the Langley 16-Foot Transonic Tunnel," NASA TM 86405, NASA Langley Research Center, 1985.

[26]Mikkelsen, K. L. and Olstad, S. J., "Airflow Calibrations of NASA Langley Research Center Multiple Critical Venturi (MCV) Assemblies," Report No. 1835, Fluidyne Engineering Corporation, June 1992.

[27]Lynn, K. C., "Development of the NTF-117S Semi-Span Balance," AIAA Paper 2010-4542, AIAA, June 2010.

[28]Lynn, K. C., Rhew, R. D., Acheson, M. J., Jones, G. S., Milholen-II, W. E., and Goodliff, S. L., "High-Reynolds Number Active Blowing Semi-Span Force Measurement System Development," AIAA Paper 2012-3318, AIAA, June 2012.

[29]Lynn, K. C., Toro, K. G., Landman, D., Chan, D. T., and Balakrishna, S., "Enhancements to the National Transonic Facility High-Reynolds Number Active Blowing Semi-Span Force Measurement System," AIAA Paper 2014-0275, AIAA, January 2014.

[30]Mercer, C. E., Berrier, B. L., Capone, F. J., and Grayston, A. M., "Data Reduction Formulas for the 16-Foot Transonic Tunnel NASA Langley Research Center (Revision 2)," NASA TM 107646, NASA Langley Research Center, July 1982.

[31]Schnell, W. C., "Axisymmetric and Non-Axisymmetric Exhaust Jet Induced-Effects on a V/STOL Vehicle Design (Part II: Analysis of Results)," NASA CR 166365, NASA Ames Research Center, January 1982.

[32]Schnell, W. C. and Grossman, R. L., "Vectoring Non-Axisymmetric Nozzle Jet Induced Effects on a V/STOL Fighter Model," AIAA Paper 1978-1080, AIAA, July 1978.

[33]Schnell, W. C. and Ordonez, G. W., "Axisymmetric and Non-Axisymmetric Exhaust Jet Induced-Effects on a V/STOL Vehicle Design (Part I: Data Presentation)," NASA CR 166146, NASA Ames Research Center, June 1981.

[34]Capone, F. J. and Bare, E. A., "Multiaxis Control Power From Thrust Vectoring for a Supersonic Fighter Aircraft Model at Mach 0.20 to 2.47," NASA TP 2712, NASA Langley Research Center, July 1987.

[35]Capone, F. J., Mason, M. L., and Leavitt, L. D., "An Experimental Investigation of Thrust Vectoring Two-Dimensional Convergent-Divergent Nozzles Installed in a Twin-Engine Fighter Model at High Angles of Attack," NASA TM 4155, NASA Langley Research Center, February 1990.

[36]Asbury, S. C. and Capone, F. J., "Multiaxis Thrust-Vectoring Characteristics of a Model Representative of the F-18 High-Alpha Research Vehicle at Angles of Attack From 0 to 70 deg," NASA TP 3531, NASA Langley Research Center, December 1995.

[37]Phelps-III, A. E., "Wind Tunnel Investigation of an Upper Surface Blown Jet-Flap Powered-Lift Configuration," NASA TN D7399, NASA Langley Research Center, December 1973.

[38]Phelps-III, A. E., "Wind Tunnel Investigation of a Twin-Engine Straight-Wing Upper-Surface Blown Jet-Flap Configuration," NASA TN D7778, NASA Langley Research Center, January 1975.

[39]Vogler, R. D., "Wind-Tunnel Investigation of Internally Blown Jet-Flap STOL Airplane Model," NASA TN D8309, NASA Langley Research Center, November 1976.

[40]Capone, F. J., "A Summary of Experimental Research on Propulsive-Lift Concepts in the Langley 16-foot Transonic Tunnel," AIAA Paper 1975-1315, AIAA, September 1975.

[41]Capone, F. J., "The Effects on Propulsion-Induced Aerodynamic Forces of Vectoring a Partial-Span Rectangular Jet at Mach Numbers from 0.40 to 1.20," NASA TN D-8039, NASA Langley Research Center, December 1975.

[42]Capone, F. J., "Effects of Nozzle Exit Location and Shape on Propulsion-Induced Aerodynamic Characteristics Due to Vectoring Twin Nozzles at Mach Numbers from 0.40 to 1.2," NASA TM X-3313, NASA Langley Research Center, January 1976.

[43]Kelly, M. W. and Tucker, J. H., "Wind-Tunnel Tests of Blowing Boundary-Layer Control with Jet Pressure Ratios up to 9.5 on the Trailing Edge Flaps of a 35 deg Sweptback Wing Airplane," NACA RM A56G19, Ames Aeronautical Laboratory, October 1956.

[44]Aoyagi, K., Falarski, M. D., and Koenig, D. G., "Wind Tunnel Investigation of a Large-Scale Upper Surface Blown-Flap Transport Model Having Two Engines," NASA TM X62296, NASA Ames Research Center, August 1973.

[45]Aoyagi, K., Falarski, M. D., and Koenig, D. G., "Wind Tunnel Investigation of a Large-Scale Upper Surface Blown-Flap Model Having Four Engines," NASA TM X62419, NASA Ames Research Center, July 1975.

[46]Jones, G. S., Milholen-II, W. E., and Goodliff, S. L., "Development of the Dual Aerodynamic Nozzle Model for the NTF Semi-Span Model Support System," AIAA Paper 2011-3170, AIAA, June 2011.

[47]Gatlin, G. M., Tomek, W. G., Payne, F. M., and Griffiths, R. C., "Recent Improvements in Semi-Span Testing at the National Transonic Facility (Invited)," AIAA Paper 2006-508, AIAA, January 2006.
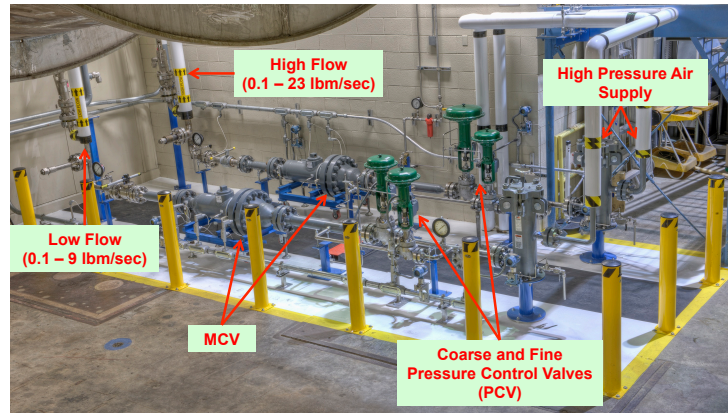
[48]Englar, R. J., Blaylock, G. M., Gaeta, R. J., Jones, G. S., and Milholen-II, W. E., "Recent Experimental Development of Circulation Control Airfoils and Pneumatic Powered-Lift Systems," AIAA Paper 2010-345, AIAA, January 2010.

[49]Rogers, E. O., "Development of Compressible Flow Similarity Concepts for Circulation Control Airfoils," AIAA Paper 1987-153, AIAA, January 1987.

[50]Abramson, J., Rogers, E. O., and Taylor, D. W., "High-Speed Characteristics of Circulation Control Airfoils," AIAA Paper 1983-265, AIAA, January 1983.

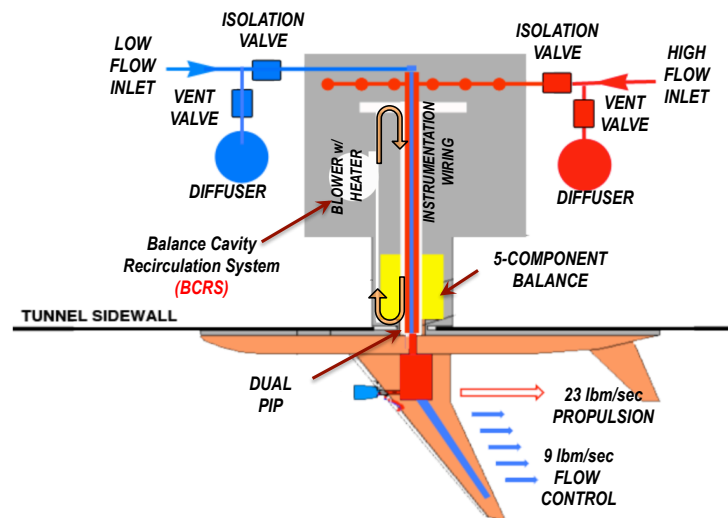# Appendix A High Pressure Air Delivery System

The NTF Air Station (Figure 26) is a high-pressure air (HPA) delivery system that provides a continuous source of clean, dry air to the test article. It obtains its dry air supply with typical dew points around -90°F from the LaRC compressor station. The dual-flow system[46] was designed to provide a cumulative weight flow rate of 32 lbm/sec between the two independent flow paths, with the low-flow path delivering up to 9 lbm/sec and the high-flow path delivering up to 23 lbm/sec. Both flow path legs are equipped with coarse and fine pressure control valves (PCV) to accurately set the desired weight flow rate. The air station has two multiple critical

Figure 26. NTF high pressure air (HPA) station with two independent flow paths capable of a combined weight flow rate of 32 lbm/sec.

venturi (MCV) systems to capture the total weight flow rate from each flow path leg. The total temperature of the HPA can be set from 20°F to 120°F by using a steam heating system. The low temperature settings are dependent on Joule Thompson effects and thermal conduction associated with the piping located in the low temperature environment of the wind tunnel plenum. The HPA station also incorporates a model protection safety system that limits the maximum pressure delivered to the model. The maximum pressure limit can be adjusted independently for both legs from 300 psi to 1200 psi. For the FAST-MAC model, a 600 psi limit at the perforated plates was established to protect the model in the unlikely event that the model flow path should experience a blockage. If the set pressure matches or exceeds the limit, then the supply line would be isolated and vented in less than 0.5 seconds.

Appendix B Sidewall Model Support System

Semi-span models in the NTF are installed on the tunnel sidewall through the Sidewall Model Support System (SMSS),[24,47] which is secured to the back side of the sidewall and located in the tunnel plenum. For propulsion and flow control simulation experiments, the HPA enters the SMSS via two independent manifolds that are connected to a rotary union before passing through the center of the force and moment balance as shown in Figure 27. The co-flowing concentric air lines transition across the balance via a high-flow and low-flow bellows and couple to the model. Each of these bellows are designed to minimize the balance tares and momentum transfer caused by the high pressure air crossing the metric/non-metric boundary of the balance. The first FAST-MAC entry utilized a convoluted bellows and the second entry utilized a Pressure Interface Piece (PIP) that is based

Figure 27. NTF SMSS showing the delivery of high pressure air to a semi-span model for propulsion and/or flow control simulations.

on the pressure characteristics of a schedule 40 pipe. The balance system calibration includes the effect of static pressure and temperature at the PIP. With this model mounting approach, the balance measures not only the aerodynamic forces and moments on the model, but also any forces generated by the pressurized

American Institute of Aeronautics and Astronautics

internal flow path inside the model and the added thrust from the blowing slot. The SMSS also provides a heated enclosure that maintains a stable temperature for the balance and the pitch mechanisms, through the use of convective heat transfer provided by the Balance Cavity Recirculation System (BCRS) closed loop control.
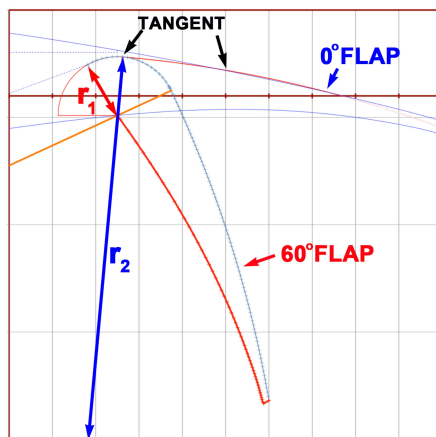
Appendix C   FAST-MAC Model

The FAST-MAC model shown in Figure 4 has a modern super-critical wing and was designed to become an NTF standard for evaluating performance characteristics of integrated active flow control and propulsion systems. The modular design and construction of the FAST-MAC model provides a capability of changing the leading edge, trailing edge, upper skin geometry (with or without engine simulators), and active or passive flow control technology. The outer mold line (OML) of the model was designed for a cruise Mach number of 0.85 and a lift coefficient of 0.50, at a Reynolds number based on mean aerodynamic chord of 30×10^6. A tangential blowing slot is located at the 85% chord location on the upper surface, and is directed over a 15% chord simple hinged flap for both the cruise and high-lift configurations.

The wing has an aspect ratio of 5.28, taper ratio of 0.40, a leading edge sweep of 30°, zero dihedral, and a reference area of 6.06 ft^2. The wing also has a twist of 5° washout that varies linearly from root to tip. The chord length at the side of the fuselage is 25.0 inches, resulting in a mean aerodynamic chord of 19.4 inches. The wing dimensions are summarized in Table 6. The generic fuselage is comprised of circular cross sections with a maximum radius of 4.0 inches, and a length of 82.0 inches. The wing is mounted in the mid-fuselage position to simplify the routing of the high-pressure air supply lines.

Table 6.   FAST-MAC model wing reference dimensions.

Parameter	Dimension
Semi-Span $(b/2)$	48 in
Reference Area (S_{ref})	6.06 ft^2
Mean Chord $(\bar{c})$	19.4 in
Aspect Ratio $(\mathcal{R})$	5.28
Tip Chord	10 in
Root Chord	25 in
Taper Ratio	0.40
Leading Edge Sweep	30°
Dihedral	0°
Twist (root to tip)	5°

The flap design philosophy used for the FAST-MAC model is based on a modified dual radius concept,[20, 48] incorporating guidelines established for circulation control airfoils having single radius Coandă surfaces with blunt trailing edges.[49, 50] The FAST-MAC dual radius flap concept (Figure 28) turns the high momentum flow over a circular radius (r_1) then takes advantage of a larger turning radius (r_2), defined by the cruise flap geometry, that keeps the flow attached along the flap as the high momentum energy is reduced. One of the critical constraints in the FAST-MAC flap design was to have the circular arc become tangent with the upper surface mold-line of the wing so that the exiting jet would be tangent to the local external flow. This determines the initial angle of the thrust vector at the slot exit.

Figure 28.   Dual radius flap definitions.[20]

American Institute of Aeronautics and Astronautics

Appendix D   Experimental Measurements

It is very important to measure the slot height to verify the desired h/c and to obtain a good calculation of the total slot area. To calculate the slot areas for each plenum, the slot height was measured at each standoff location along the span of the slot using precision pin gauges. The repeatability for this type of measurement is dependent on the "feel" of the measurement technician and industry standards characterize the accepted error to be ± 0.0005 inches. The measurements for the $0°$ cruise flap are shown in Figure 29. The ends of the aft plenum cover are fixed and the slot height at those locations cannot be adjusted with shims, but the majority of the slot is at the desired height. This was true for all flap configurations.
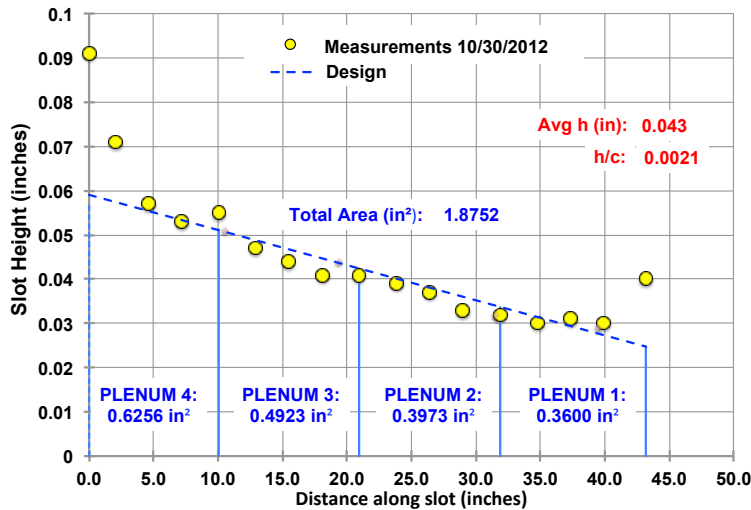

Figure 29. Slot height measurements along the span of the slot for the $0°$ cruise flap.

The MCV weight flow rate measurement systems can accommodate up to 44 lbm/sec of air at a maximum inlet pressure of 1500 psi. As shown in Figure 30, the system inlet flow is distributed uniformly into a common plenum by a radial inlet diffuser and a large perforated plate. The flow then passes through a combination of calibrated venturis before exiting the system. The venturis vary in size in binary increments of throat area so that each successively larger venturi passes twice the flow of the preceding one. The unused venturis are capped to force all of the flow through the remaining venturis. The combined uncertainty of the MCV system is reported to be less than 0.35 percent of reading.
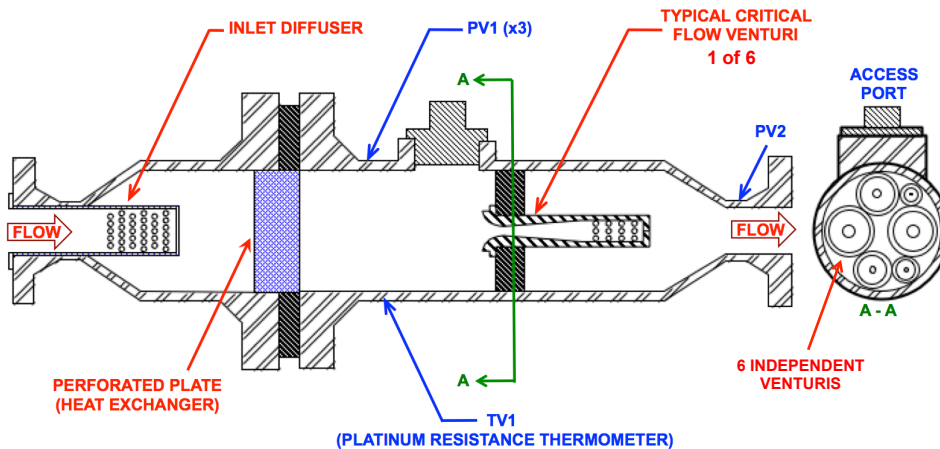

Figure 30. Multiple Critical Venturi (MCV) weight flow rate measurement system.

American Institute of Aeronautics and Astronautics

The NTF-117S balance shown in Figure 31 is a large 5-component (no side force measurement capability) strain gauge balance that is mounted inside the SMSS and is the primary force measurement system for semi-span models in the NTF. The PIP interface allows the high-pressure supply air needed for propulsion and flow control simulation testing to "bridge" the balance by crossing from the non-metric end to the metric end. This means that the thrust produced by the flowing air is sensed and measured by the balance. Figure 32 shows a cross section of the SMSS and details of the area around the PIP. When the PIP experiences pressure and temperature variations due to the flowing air, it can change the characteristics of the balance, since the PIP can essentially be modeled as a large spring with varying spring constants. Consequently, the balance and PIP must be considered together as a <u>system</u> and calibrated accordingly.
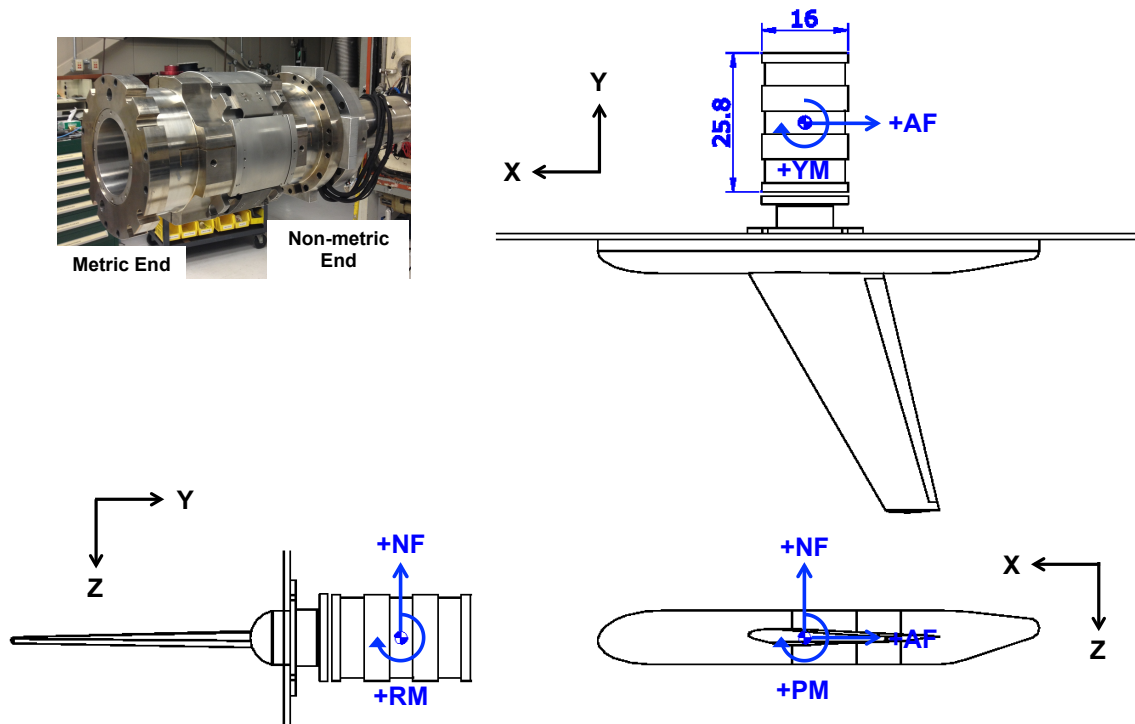

Figure 31. NTF-117S five-component strain gauge balance.

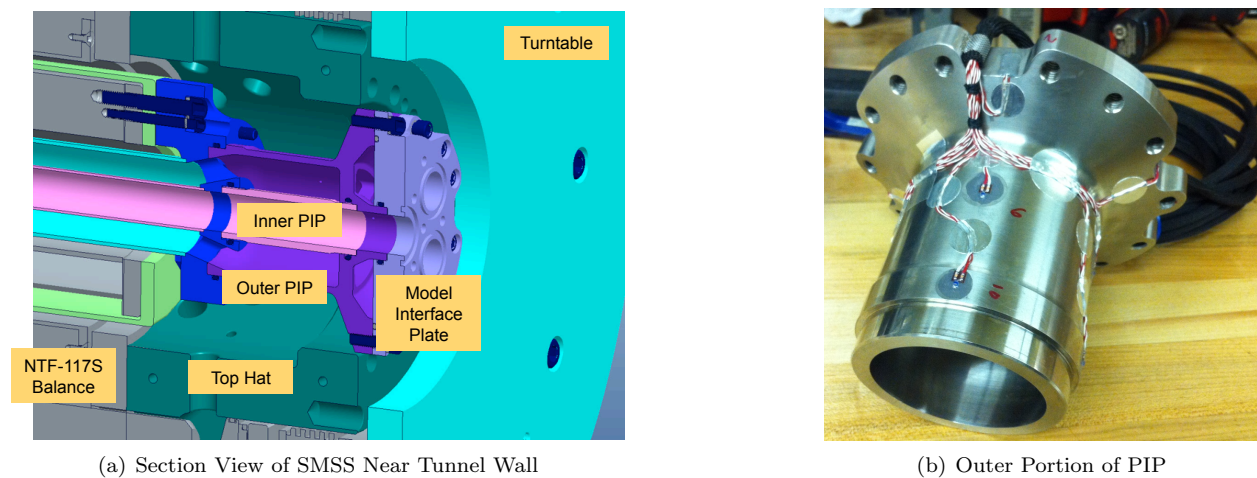(a) Section View of SMSS Near Tunnel Wall

(b) Outer Portion of PIP

Figure 32. Cross section view of SMSS showing NTF-117S balance and PIP interface.

American Institute of Aeronautics and Astronautics